applied sciences

MDPI

Article

Dimensional Analysis and Unified Ultimate Bearing Capacity Expression for I-Wing Piles in Loess: Experimental and Numerical Study

Fanli Tang [1], Gang Zhao [1], Peng Zhang [1], Yuhang Guo [1], Fan Wen [2] and Qing Sun [3,*]

[1] State Grid Shaanxi Electric Power Company Economic and Technological Research Institute, Xi'an 710065, China
[2] Northwest Electric Power Design Institute Co., Ltd. of China Power Engineering Consulting Group, Xi'an 710075, China
[3] Department of Civil Engineering, Xi'an Jiaotong University, Xi'an 710049, China
* Correspondence: sunq@mail.xjtu.edu.cn

Abstract

Transmission tower foundations in China's collapsible loess plateau face severe settlement risks under sustained vertical compression, yet the compressive behavior of winged piles in this metastable soil remains unexplored. This study presents a combined experimental and numerical investigation of I-wing piles in remolded Malan loess, comprising plain (WP0), two-wing (WP2), and four-wing (WP4) configurations. Three-dimensional finite-element models were validated against physical load tests and subsequently used to decompose load transfer into toe, wing-bearing, and side components via a unified hyperbolic interface model. A sixteen-case parametric study isolated the effects of wing geometry and soil properties, and the complete dataset was synthesized into a unified dimensionless capacity expression using Buckingham π theorem. At a normalized settlement of $s = 0.1d$, the four-wing pile (WP4) exhibited a 69% increase in compressive capacity compared with the plain pile (WP0) in the validated finite-element simulations, while the corresponding physical tests showed a 52% increase. The proportion of pile-base resistance decreased from 59.65% for WP0 to 33.18% for WP4. For WP4, wing-bearing resistance accounted for 18.98% of the total capacity, while total side resistance contributed the largest share at 47.85%. The two-wing pile (WP2) showed capacity increases of 43% in the finite-element simulations and 36% in the physical tests. The investigated reduced-scale baseline had its highest capacity near $h_w/d \approx 1.3$, an optimum observed only under the investigated soil and geometric conditions. The hyperbolic model captures all interface responses with R^2 spanning 0.933 to 0.999. The derived formula achieves an in-sample MAPE of 3.37%, a leave-one-out cross-validation MAPE of 4.66%, and eight independent finite-element blind predictions (full-scale and intermediate-scale prototype winged-pile configurations) within −4.4% to +3.4% (MAPE = 2.63%). Scale calibration used only one numerical monopile reference (FS-M); the eight cases are finite-element predictions, not field tests. Geometric and material similarity are preserved, but strict stress similarity is not achieved under 1 g conditions; the explicit gravity correction factor G represents this mismatch within the investigated numerical domain. These findings demonstrate that winged piles effectively redistribute compressive load away from the pile toe in loess, and the proposed unified expression provides a preliminary prediction tool numerically assessed within the investigated models and parameter ranges for dry, remolded loess.

Check for updates

Academic Editor: Marco Zucca

Received: 21 August 2026
Revised: 19 October 2026
Accepted: 27 October 2026
Published: 5 November 2026

Copyright: © 2026 by the authors. Licensee MDPI, Basel, Switzerland. This article is an open access article distributed under the terms and conditions of the Creative Commons Attribution (CC BY) license.

Keywords: winged pile; Malan loess; transmission tower; load transfer mechanism; hyperbolic model; Buckingham π theorem

1. Introduction

The rapid expansion of high-voltage transmission networks across Northwest China, driven by the region's growing energy demand and the west-to-east power transmission strategy, is placing unprecedented demands on tower foundation engineering [1–3]. Unlike standard building foundations, these structures must resist a complex, simultaneous combination of forces: lateral wind pressure, uplift from cable tension, and sustained vertical compression from the tower's own weight and ice accumulation. While this compressive load is ever-present and dictates the foundation's size under normal service conditions, it remains surprisingly under-researched in the literature on special-shaped piles, which traditionally focuses on lateral or uplift resistance. The consequences of inadequate compressive support are severe. The back-analysis of real-world tower failures reveals that structural damage begins at foundation settlements as small as 10–50 mm, with catastrophic collapse following at just 120–170 mm [4]. Therefore, as transmission corridors push deeper into loess terrain, developing innovative designs that deliver high compressive capacity while minimizing material costs is an urgent engineering priority.

Covering over 640,000 km^2 with deposits up to 400 m thick, collapsible loess defines the landscape of northwest China's Loess Plateau [5,6]. A substantial share of these transmission corridors traverses the Loess Plateau, where the metastable, collapsible structure of Malan loess poses persistent challenges to foundation safety and long-term settlement control [5,6]. It is important to note that the material investigated herein is geologically classified as collapsible Malan loess; however, the present study examines dry, remolded, and compacted specimens only, with wetting-induced collapse, suction loss, and negative skin friction excluded from the current scope. Moisture infiltration poses a severe threat to loess foundations, as it can reverse the direction of shaft resistance. When self-weight collapsible loess gets wet, the resulting soil collapse creates negative skin friction that pulls the pile downward, drastically reducing compressive capacity and potentially causing total failure [7]. Experimental and numerical studies have examined axial load transfer and shaft resistance in pile foundations, including the effects of loess collapse on pile–soil interaction [8–10]. More recent work has expanded to evaluate screw piles [11] and transmission tower pile groups under flooded conditions [12]. Nearly all these studies focus exclusively on conventional, plain circular shafts. Conventional foundation methods simply struggle in collapsible loess regions. Because the upper 8–9 m of Malan loess is intensely collapsible (collapse coefficient > 0.09 at 1 m) [13,14], rainfall infiltration can cause footings to abruptly sink by 30–50 cm [5]. Straight-shaft bored piles offer an alternative, but they must be driven 15–25 m deep just to generate enough friction. Even then, they rely on a single resistance mechanism that weakens rapidly when the soil gets wet. These severe limitations point to a clear need for wing-plate piles, which add supplementary bearing components to safely boost load capacity without requiring impractically deep excavation.

To achieve higher capacity, a well-proven strategy is to enlarge the pile's soil contact area by adding bearing elements to the shaft. Belled and under-reamed piles have utilized this principle since the 1960s [15]. Today, modern finned, winged, screw, and root piles have demonstrated capacity gains of 30% to over 200% relative to plain piles in sand and clay [16–18]. Fins can improve lateral pile resistance, while the uplift and lateral performance of helical pile groups depends on their geometry and configuration [19,20]. Importantly, enlarged-bearing concepts are also viable in loess ground, as evidenced by the successful

load testing of a squeezed branch-and-plate pile in fully immersed collapsible loess [21]. Finally, evidence suggests that simple rectangular fins perform just as well as elaborate tapered shapes [16], ensuring that the winged pile remains both highly effective and easy to fabricate.

The methodologies for analyzing special-shaped piles are robust and well documented. Pairing physical laboratory tests with finite-element simulations has become the standard analytical approach [22–26]. Because these piles often do not exhibit a distinct plunging failure, ultimate capacity is typically defined using a settlement threshold of 10% of the pile diameter—a long-standing criterion utilized in current design codes [27,28]. Dimensional analysis based on the Buckingham π theorem provides a framework for identifying governing dimensionless groups and expressing pile responses in normalized form [29–32].

Despite this extensive background, three critical knowledge gaps remain. First, to the authors' knowledge, winged piles have never been tested in collapsible Malan loess. Existing winged-pile research is restricted to sand and clay, while loess foundation studies focus almost exclusively on conventional, plain shafts. Second, the literature on special-shaped piles heavily prioritizes lateral and uplift resistance. Consequently, the systematic compressive behavior of winged piles—the primary load case governing transmission tower service conditions—remains largely unexplored. Third, current capacity predictions for winged piles are entirely case-specific. There is currently no unified, dimensionless equation that links ultimate capacity to key wing geometries (number, projection, and height), even though the Buckingham π theorem provides the perfect framework to develop one.

This study bridges existing research gaps through a combined experimental and numerical investigation of I-wing piles under vertical compression in remolded Malan loess. Three physical model configurations a plain baseline pile—(WP0), a two-wing pile (WP2), and a four-wing pile (WP4)—were tested, and corresponding 3D finite-element models were developed and validated against the experimental load settlement data and failure patterns. Acting as virtual instruments, these models explicitly decomposed the internal load transfer into toe, wing-bearing, and side components using a calibrated, unified hyperbolic interface mode. Subsequently, a sixteen-case parametric study evaluated the structural influence of seven key variables: wing number, wing projection, wing height, pile length, soil cohesion, elastic modulus, and wing embedment. Applying the Buckingham π theorem and nonlinear regression to this comprehensive database yielded a unified dimensionless expression for the ultimate compressive capacity of winged piles, whose predictive performance was assessed by leave-one-out cross-validation and eight prototype-scale finite-element predictions within the investigated numerical domain, with one numerical monopile reference reserved for scale calibration.

2. Materials and Methods

2.1. Physical Model Test

To simulate prototype foundation behavior in Malan loess while accommodating laboratory constraints, reduced-scale physical models were constructed. The main pile bodies were cast from C25-grade normal-weight concrete, while the transverse wing plates were fabricated from Q235B structural steel. Designed to fundamentally enhance the pile's total ultimate bearing capacity, the wing plates feature a miniature I-beam cross-section with a 45° tapered tip to ensure smooth soil penetration and minimize stress concentrations during installation. Each wing was cast monolithically into the concrete shaft, with a specific radial projection ($0.45d$) chosen based on prior parametric studies indicating diminishing returns for projection ratios beyond $0.4d$–$0.5d$. The detailed geometric and material parameters used for manufacturing the physical specimens that also serve as the baseline inputs for the subsequent finite element model validation (Section 2.2) are summarized in Table 1.

Table 1. Geometric and material properties of the concrete pile and steel wing plate models.

Component	Parameter	Value
Concrete Pile (C25)	Diameter (d)	100 mm
	Embedded Length (L)	1200 mm
	Elastic Modulus (E_c)	28 GPa
	Mass Density (ρ_c)	2446 kg/m^3
	Poisson's Ratio	0.3
Steel Wing Plate (Q235B)	Yield Strength (f_y)	235 MPa
	Wing Height (h)	36 mm
	Flange Width (b_f)	14 mm
	Web Thickness (t_w)	1.5 mm
	Total Wing Length (B_w)	65 mm
	Wing Embedded (B_{emb})	20 mm
	Wing Projection (B)	45 mm ($0.45d$)

The primary geometric parameters of the baseline foundation model are defined schematically in Figure 1. The cylindrical pile shaft has a diameter of $d = 100$ mm and an embedded length of $L = 1200$ mm (slenderness ratio $L/d = 12$). Each of the $n = 4$ wings consists of an I-section structural steel fin (grade Q235B) with a flange width of $b_f = 14$ mm, a web thickness of $t_w = 1.5$ mm, and a section height of $h = 36$ mm, welded radially and orthogonally to the shaft circumference. The total radial wing length of $B_w = 65$ mm comprises an exposed radial projection of $B = 45$ mm and an embedded root segment of $B_{emb} = 20$ mm. The wing's centerline sits at an embedment depth of $h_w = 130$ mm below the ground surface, corresponding to a normalized embedment ratio of $h_w/d = 1.3$. It is emphasized that the wing section height (h) and the wing centroidal embedment depth (h_w) represent distinct physical dimensions, and are treated as independent parameters throughout this formulation. The scaling of reduced-scale experimental behavior to prototype foundations is considered through the similitude framework detailed in Section 3.6, which identifies the gravity-stress ratio (π_8) as the sole dimensionless group that cannot be replicated in a 1 g physical model, and formulates an explicit scaling correction within the capacity equation. Furthermore, Section 4.4 provides eight prototype-scale finite-element comparisons within the investigated domain; scale calibration uses one numerical monopile reference. These comparisons are not full-scale field tests.

To ensure the reliability of the model tests and eliminate boundary effects, experiments were conducted in a rigid steel-reinforced concrete tank measuring 3.0 m(L) × 2.4 m(W) × 3.0 m(H), as shown in Figure 2b. These dimensions provide a horizontal clearance exceeding $10d$ between the pile surface and the tank walls. Additionally, to prevent moisture exchange with the surrounding environment, the tank's interior was fully lined with 3 mm-thick polyethylene sheeting. Site-sampled loess soil, Figure 2a, was meticulously prepared in the laboratory to replicate field conditions. The soil was placed in the tank in controlled 150 mm-thick loose layers, with each layer compacted using a vibrating plate compactor yielding a constant unit weight (γ) of 17 kN/m^3. By filling the tank to its full 3.0 m capacity, the 1.2 m-long piles were underlain by 1.8 m of compacted foundation soil, successfully preventing any boundary-induced base effects. Comprehensive physical properties of the loess soil are provided in Table 2.

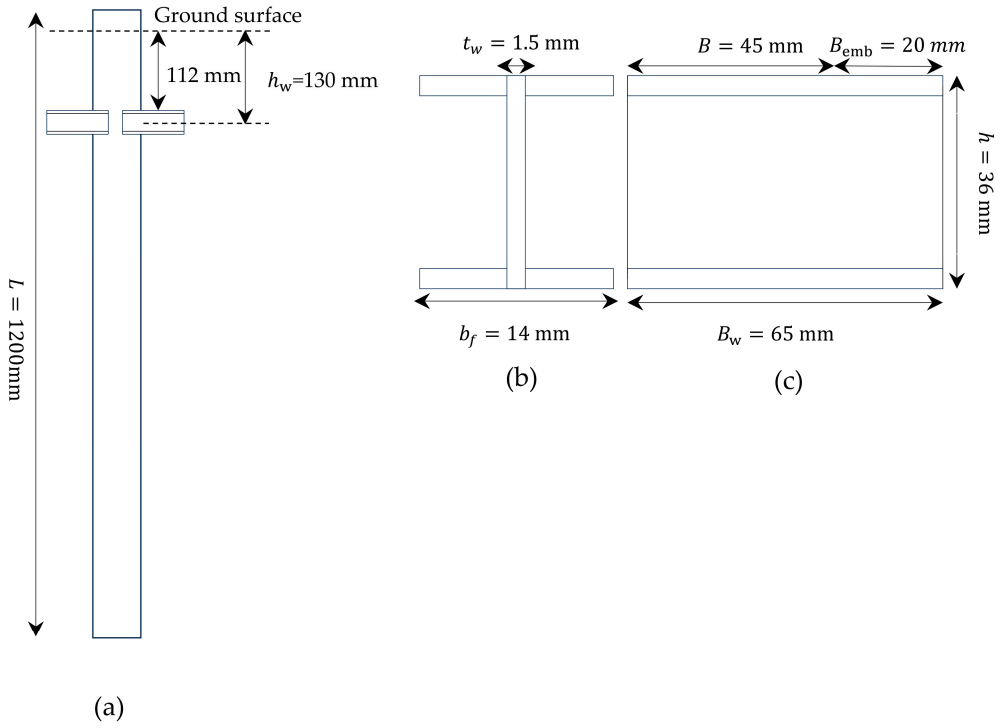


Figure 1. Geometry and notation of the I-wing pile: (**a**) elevation; (**b**) wing cross-section; (**c**) wing plan.



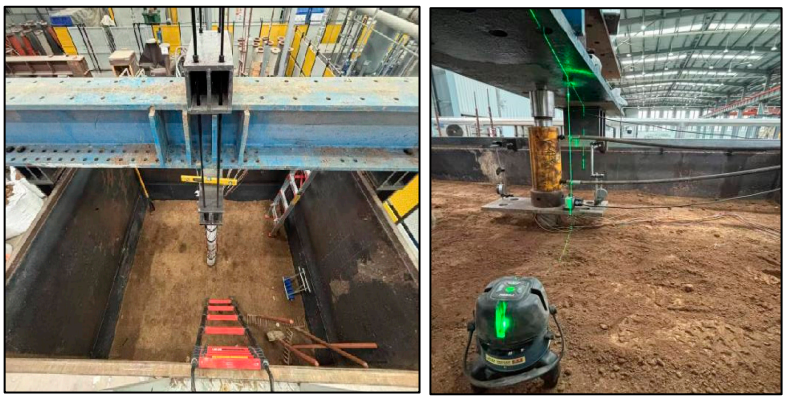
Figure 2. (**a**) Loess soil collected from site. (**b**) Preparation of soil container box for model test.

Table 2. Experimental parameters of loess soil.

ρ/(g/cm^3)	c/(kPa)	E_s/(MPa)	w/(%)	φ/(°)
1.7	15.5	20	20.04	20

The load was applied through a 500 kN capacity hydraulic jack reacting against a rigid steel beam, with the applied load measured by a calibrated load cell (Figure 3). All pile specimens were subjected to vertical compressive loading under load-controlled conditions following the maintained load test procedure specified in Chinese code [33]. Loading continued until one of the following failure criteria was satisfied: (a) pile head settlement exceeded 0.1d (10 mm) under a given load increment; (b) the load-settlement curve exhibited a clearly defined peak followed by sustained load reduction; or (c) the settlement rate under constant load showed no sign of deceleration after 30 min. The

applied load and corresponding settlement were simultaneously recorded using the Test Master load acquisition software, which displays and logs the load displacement response throughout the test (Figure 4).



(**a**) (**b**)

Figure 3. Experimental setup for the vertical pile load test: (**a**) installation phase showing the pile suspended from the reaction beam during the initial soil filling stage; (**b**) execution phase displaying the hydraulic jack, load transfer plates, displacement gauge.



(**a**) (**b**)

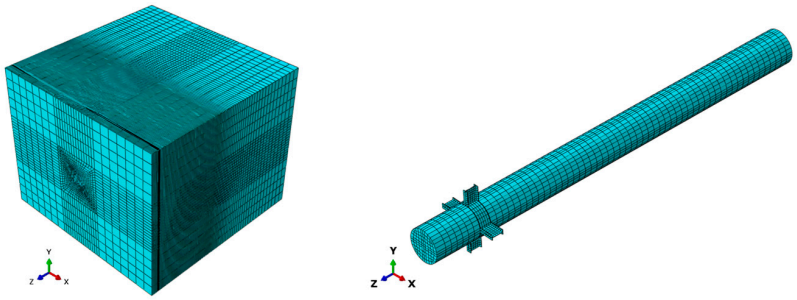
Figure 4. Test control apparatus: (**a**) data acquisition computers; (**b**) hydraulic pump station for vertical loading.

2.2. Numerical Simulation Using Finite Element Method

Three-dimensional finite-element analyses were performed using ABAQUS/Standard version 2025. Two sets of models were constructed: (1) validation-scale models replicating the exact geometry of the physical test specimens as per Table 1 for direct comparison with the measured load–settlement curves; and (2) parametric models for the wing geometry study of Section 3.5, constructed at the same scale so that the experimental configurations sit within the parametric matrix as anchor cases. Because the wings break the axial symmetry of the pile, no axisymmetric idealization is admissible. As shown in a previous study by Tolun et al. [34], a finer mesh density increases analysis time, and also there is no more difference in the result, so mesh refinement was concentrated in the vicinity of the pile shaft and wing plates, with element sizes graduating from 30 mm near the interfaces to 100 mm at the far-field boundary; at least five elements were maintained across the wing height and 10 elements across wing length to resolve the contact tractions used in the load transfer decomposition, and the model is discretized using 3D eight node brick elements with reduced integration (Table 3). The mesh model can be seen in Figure 5.

Table 3. Mesh convergence study on the baseline WP4 model; capacity evaluated at $s = 0.1d = 10$ mm.

Mesh Level	Near Seed (m)	Far Seed (m)	Nodes	Elements	Q (kN)	ΔQ vs. Fine (%)
Coarse	0.06	0.20	107,601	103,644	9.06	+8.1
Medium (Baseline)	0.03	0.03–0.10	159,257	153,305	8.68	+3.6
Fine	0.02	0.02–0.1	204,167	196,450	8.38	-



3D soil domain and boundary mesh Structural mesh of 4-wing pile

Figure 5. Meshing of pile–wing–soil model.

To verify numerical objectivity and minimize spatial discretization sensitivity to within an acceptable tolerance, a dedicated mesh convergence study was performed on the baseline four-wing foundation model (Table 3). Three soil mesh densities—coarse, medium, and fine—were evaluated while maintaining identical continuum element types (C3D8R), kinematic boundary conditions, and wing discretization. Specifically, the wing mesh was held constant at 5 elements along the wing height and 10 elements along its radial length, comprising 6 elements across the exposed 45 mm wing face and 4 elements across the 20 mm embedded root portion. Only the soil domain was refined, with characteristic element seeding in the near-field zone set to 0.06 m, 0.03 m, and 0.02 m (corresponding to $0.6d$, $0.3d$, and $0.2d$), respectively. The computed vertical compressive capacity at the serviceability limit ($s = 0.1d$) decreased monotonically with mesh refinement, yielding 9.06 kN (coarse), 8.68 kN (medium), and 8.38 kN (fine). The relative difference between the medium and fine meshes was 3.6%, which falls safely within the widely accepted 5% convergence threshold. Consequently, to maintain an optimal balance between numerical precision and computational economy, the medium mesh discretization was adopted for all subsequent simulations reported herein.

The soil domain extended to $15d$ and $12d$ laterally from the pile axis in the x- and y-directions, respectively, and $18d$ below the pile toe ($d = 100$ mm), consistent with established recommendations for eliminating boundary effects in axially loaded pile analyses [34–36], and the lateral boundaries were restrained in the normal direction (roller condition) and the base was fully encased, replicating the confinement conditions of the laboratory test box as shown in Figure 6a. For the Abaqus simulations, the remolded Malan loess was modeled using an elastic–perfectly plastic Mohr–Coulomb framework. It is noted that the Mohr–Coulomb framework adopted herein models dry, compacted loess under the investigated working conditions; it does not simulate wetting-induced collapse, suction loss, or negative skin friction. A Poisson's ratio of $\mu = 0.35$ was assigned to the loess, consistent with the reported range of 0.30–0.35 adopted for Malan loess in numerical studies [37]. Furthermore, the minimum admissible dilation angle was $\psi = 0.1°$, reflecting the negligible dilatancy of loose, contractive silty soils [38,39]; this is a constitutive modeling choice based on the contractive behavior of the remolded loess and has likewise been adopted in finite-

element studies of winged piles and anchors in silty soils [26]. It should be emphasized that the present study is bounded by the investigation of reconstituted, non-inundated Malan loess. The elastic–perfectly plastic Mohr–Coulomb framework adopted herein does not account for wetting-induced hydro-mechanical phenomena such as structural collapse, matric suction dissipation, or down-drag (negative skin friction), which represent critical behavioral characteristics of unsaturated loessial deposits subjected to environmental infiltration. Consequently, the experimental observations, numerical calibrations, and resulting design formulations presented in this paper are established under as-compacted, non-wetted soil conditions. Advanced hydro-mechanically coupled constitutive modeling and experimental load testing under controlled water infiltration represent essential avenues for future research before extending the proposed design expressions to foundations in collapsible or wetting-susceptible loess environments.

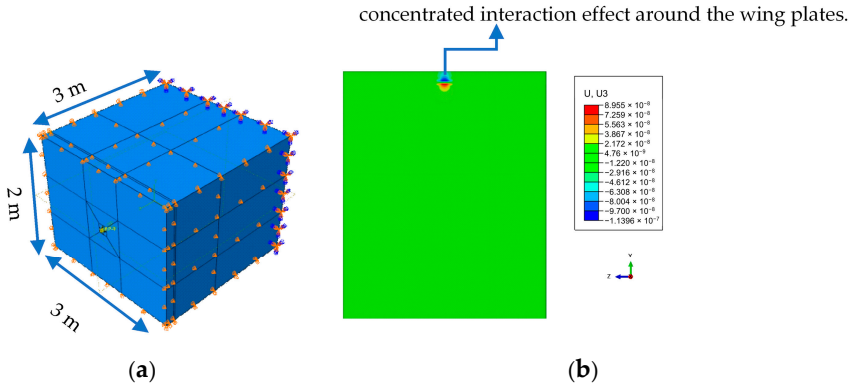


Figure 6. Finite element model setup and initial stress state: (**a**) configuration of the soil domain and boundary conditions; (**b**) verification of geostatic equilibrium, demonstrating near-zero vertical displacements (U3) across the pile–wing–soil interaction zone.

The remolded soil was completely isotropic and homogeneous during each test. The Mohr–Coulomb model is widely adopted for simulating the complex mechanical behavior of soils, including loessial soils, due to its computational efficiency and general accuracy in predicting shear failure and foundation stability [36,40,41]. The structural elements were modeled as linear elastic materials in accordance with Chinese national standards [42,43]. The C25-grade concrete pile was assigned to a Young's modulus of 28 GPa, a Poisson's ratio of 0.30, and a unit weight of 25 kN/m^3. The Q235-grade steel wing plates were defined as a modulus of 206 GPa and a Poisson's ratio of 0.30. Preliminary analyses confirmed that all structural components remain strictly within the elastic regime throughout the loading sequence, precluding the need to model plate yielding. To replicate the welded physical specimens, the 20 mm portion of wing was simulated using an embedded-region constraint, which rigidly anchors the wing plates within the concrete shaft, and the remaining 45 mm with pile shaft was simulated using surface–surface interaction.

Load transfer at the foundation–soil interface was defined in both the normal and tangential directions. Normal interaction was governed by a "hard" contact formulation, ensuring that compressive forces are only transmitted when the structural and soil surfaces are in direct physical contact. Tangential interface behavior was governed by the classical Coulomb friction law, and a uniform friction coefficient of $\mu = 0.40$ was back-calibrated by matching the measured load-settlement response of the plain monopile (WP0). Table 4 summarizes the computed ultimate bearing capacities of the three pile configurations. Because the same soil bed preparation protocol (compaction to 1.75 g/cm^3) was used for all three test configurations, a single calibrated $\mu = 0.40$ consistently reproduced the measured capacity rankings across concrete–shaft and steel–wing interfaces (errors $\leq$ 6%, as shown

in Section 3.3.2), justifying its unified application. Adopting an identical coefficient across both materials is justified by the comparable interface shear mobilized along cast concrete and a rolled steel finish of similar roughness. Furthermore, this selection is corroborated by direct validation against the physical load tests, wherein the steel wings interacted with the same remolded Malan loess under an identical controlled preparation procedure (see Section 3.3.2) [36,44,45]. Furthermore, to properly resolve the significant disparity in stiffness between the rigid structural components and the deformable loess, a master–slave contact algorithm was implemented. Specifically, the stiffer pile and wing surfaces were designated as the master surfaces, while the softer surrounding soil was assigned as the slave surface [36]. An initial geostatic step was executed in Abaqus using the automatic balance method to establish the in situ stress state. This procedure verifies that the predefined stress field perfectly counterbalances both the gravitational loads and the boundary constraints. As demonstrated in Figure 6b, the maximum vertical displacement (U3) following this initialization was on the order of 10^{-7} m. This value is significantly lower than the widely accepted 10^{-4} m tolerance threshold for geotechnical engineering practice, confirming a successfully balanced model prior to external loading [46,47].

3. Results and Discussion

3.1. Load–Settlement Response of Model Piles

Figure 7 shows the load–settlement curves of the three model piles obtained from the finite element analyses: the plain pile (WP0), the two-wing pile (WP2), and the four-wing pile (WP4). All three piles behave in a similar way—the response is almost linear at the beginning and then gradually softens as the load increases, with no clear failure point up to a settlement of 10 mm. This gradual, hardening-type behavior is typical of piles in remolded loess, where shaft friction and toe resistance build up progressively rather than failing suddenly. The wings clearly improve both the stiffness and the capacity of the pile. The initial stiffness increases from 2.15 kN/mm for WP0 to 2.97 and 3.20 kN/mm for WP2 and WP4, i.e., gains of about 38% and 49%. The winged piles also begin to soften at slightly higher loads than the plain pile, indicating wings delay the progressive mobilization of the surrounding soil. At any given settlement, the four-wing pile carries the maximum load and the plain pile the lowest, which can be seen over the whole displacement range. Since the curves never reach a distinct failure point, a displacement-based criterion is needed to compare their capacities consistently. The ultimate capacities extracted from these curves at a settlement of 10% of pile diameter are presented and discussed in Section 3.2.

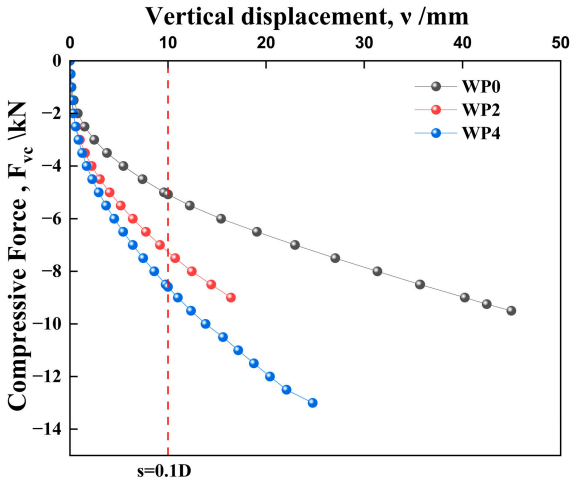


Figure 7. Load settlement curve using the load-controlled finite element method.

3.2. Ultimate Bearing Capacity and Wing Number Effect

The ultimate compressive capacity Q_u was defined as the load corresponding to a pile head settlement equal to 10% of the pile diameter (s_u = 10 mm), following the criterion originally proposed by Terzaghi [27], adopted in foundation design codes IS 2911 (Part 4): 2013 [28], and widely applied in model-scale pile studies [48–51]. At the reference settlement of $s = 0.1d$ = 10 mm, the piles carry 5.08, 7.27, and 8.59 kN, respectively; the two-wing pile carries 43% more than the plain pile, and the four-wing pile 69% more. This benefit, however, does not grow linearly with the number of wings. Going from two to four wings adds only a further 18.2%, and the gain per wing drops from 21.5% to 17.3%. The reason is that neighboring wings activate partly the same volume of soil, so each additional wing contributes less than the previous one. Table 4 summarizes the ultimate capacities and improvement factors (IF = Q_u(winged)/Q_u(plain)) obtained from the finite-element analyses; adding two wings raises the capacity from 5.08 kN to 7.27 kN (IF = 1.43), and adding four wings raises it to 8.59 kN (IF = 1.69). The corresponding measured capacities (see Section 3.3.2) confirm the ranking, with the models bounded by the validation errors.

Table 4. Ultimate capacities of the model piles at $s = 0.1d$ (load-controlled numerical results of the validated finite-element analyses).

Model	Number of Wings (n)	Q_u at s = 10 mm (kN)	Improvement Factor (IF)
WP0	0	5.08	1.00
WP2	2	7.27	1.43
WP4	4	8.59	1.69

The wings generate additional capacity through two new mechanisms, namely, direct bearing on the wing plates and an increased shaft–soil contact area (detailed in Section 3.4.2). However, this structural enhancement yields diminishing returns. Doubling the wing count from two to four increases the ultimate capacity (Q_u) by merely 19.4%, lowering the average per-wing contribution from 21.5% to 17.3%. This happens because the stress zones of closely spaced wings begin to overlap, reducing the effective volume of soil that each subsequent wing can mobilize.

3.3. Validation of Model

3.3.1. Soil Failure Mechanism Comparison and Interpretation

The finite element simulations provide a detailed look into the physical failure mechanisms within the soil. Figure 8 illustrates the contours of maximum principal plastic strain (PE) at the final loading step alongside post-test photographs of the excavated pile heads. In the plain pile (WP0), plastic yielding is isolated to a compact bulb directly beneath the toe; the surrounding loess remains essentially elastic, relying entirely on standard shaft friction and toe bearing. The winged piles (WP2 and WP4), however, trigger additional plastic zones that extend outward from the wing tips, proving that the wings successfully engage the surrounding soil via direct bearing. Yet, as seen in the WP4 section of Figure 8, adding four wings causes the individual plastic zones to overlap and coalesce. This forces adjacent wings to rely on the same shared volume of mobilized soil, directly confirming the mechanical cause behind the diminishing per-wing capacity gains detailed in Section 3.2.

The vertical stress (S33) distributions shown in Figure 9 further validate this load transfer mechanism. For the plain pile (WP0), load diffuses primarily through a concentrated stress bulb beneath the toe, with stresses decaying rapidly along the shaft. In contrast, the winged piles (WP2 and WP4) develop prominent stress concentrations at the wing locations. By transferring significant loads directly into the shallower soil through bearing,

the wings substantially reduce the intensity of the toe stress bulb. Furthermore, as the wing count increases to four (WP4), the individual stress zones merge into one continuously loaded region. This structural overlap mirrors the plastic zone coalescence observed earlier, proving that adjacent wings share a mobilized soil volume.

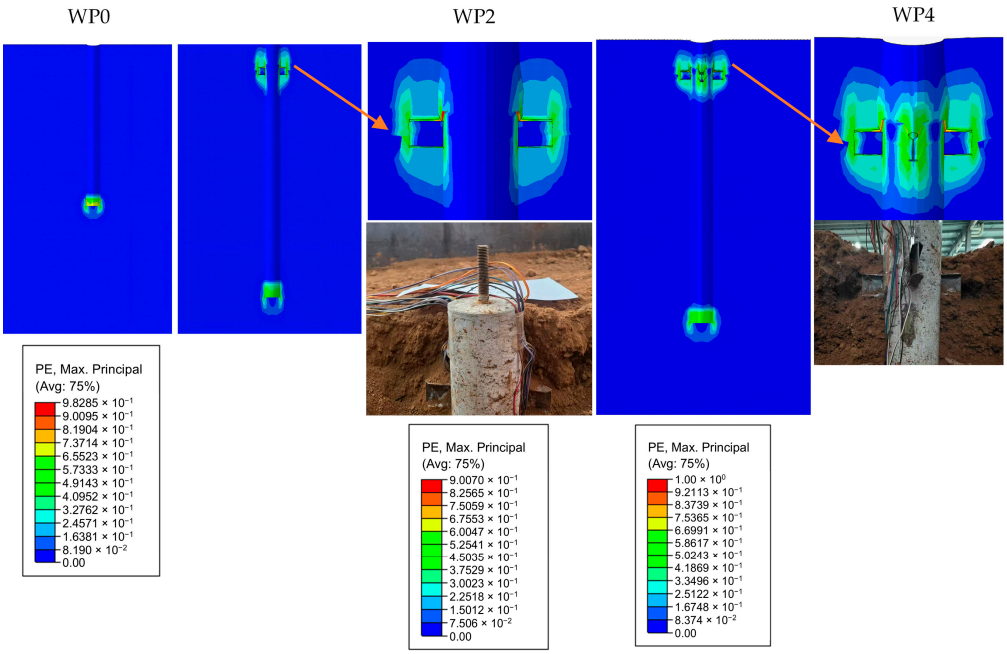


Figure 8. Comparison between simulation plastic strain contours and physical test failure pattern at maximum load applied.

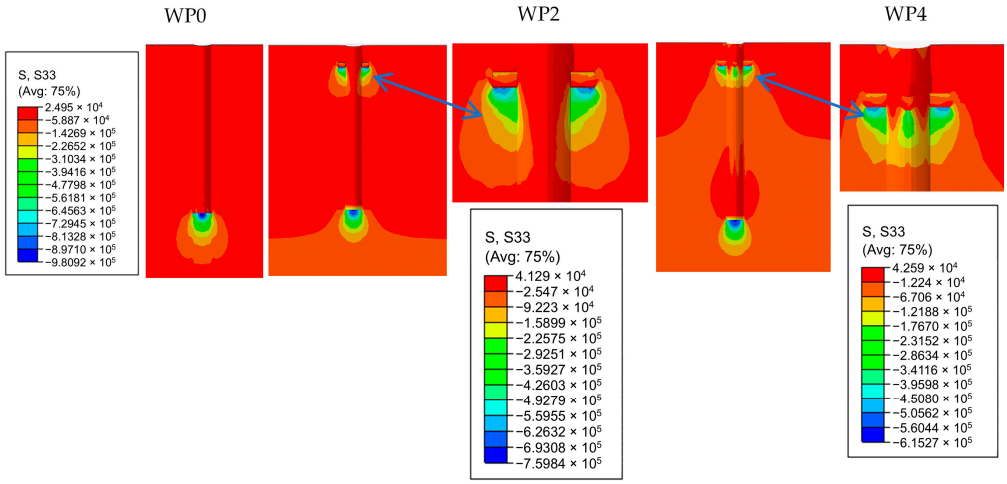


Figure 9. FEM S33 results for model tests under maximum applied load.

3.3.2. Prediction of Load–Settlement Curve

The Finite Element Models were validated against three physical model tests by comparing the computed and measured load–displacement curve as in Figure 10, following the established practice of curve-based validation for pile models [52]. So to match the experimental conditions as closely as possible, and within a certain allowable error, the validation analysis used the same load-controlled procedure as laboratory tests. Accordingly, two model variants were prepared for each configuration: a load-controlled model, adopted for the capacity comparison with the tests, and a displacement-controlled model, used for curve-shape verification and as the basis of the parametric study (Section 3.5). The numer-

ical simulation is necessarily idealized, whereas the experiments involved uncontrolled factors; in particular, the soil box was emptied and refilled for each test, so identical soil conditions could not be guaranteed from batch to batch. Nevertheless, the computed and measured load–settlement curves agree closely.

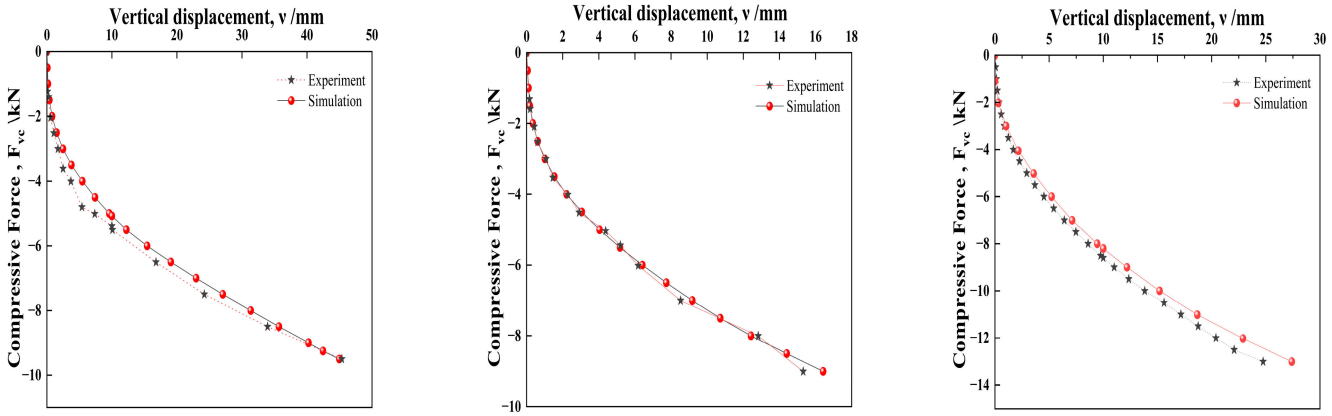


Figure 10. Comparison of experimental and load-controlled numerical simulation load–settlement curves.

From Table 5, it can clearly be seen that the relative errors of numerical simulation results at $s = 0.1d$ were below 10%, which validated the accuracy of the finite element method.

Table 5. Comparison of experimental and numerical simulation values at $s = 0.1d$.

Model Pile	Simulation (kN)	Experiment (kN)	Maximum Error at $s = 0.1d$
WP0	5.08	5.387	−5.69%
WP2	7.27	7.34	−0.95%
WP4	8.59	8.20	+4.75%

The loading protocol applied uniform load increments of 1 kN, with ultimate capacity extracted at the normalized settlement threshold of $s = 0.1d$. Displacements were monitored using two independent precision dial gauges (0.01 mm resolution) mounted symmetrically on diametrically opposite sides of the pile head. The maximum gauge-to-gauge discrepancy recorded throughout testing was 0.36 mm (i.e., ≤3.6% of the 10 mm criterion displacement), confirming axisymmetric load transfer and negligible shaft eccentricity within each test. Soil beds were reconstituted under a standardized compaction protocol targeting a dry density of 1.75 g/cm^3.

An engineering uncertainty budget following GUM principles assumes independent components: (i) load discretization ($u_1 = 0.289$ kN), (ii) displacement measurement ($u_2 = 0.18$ kN), and (iii) soil bed preparation variability ($u_3 = 0.410$ kN, inferred from FE validation scatter as 6% of the mean experimental capacity of 6.84 kN). Combination assuming independence yields

$$u_c = \sqrt{u_1^2 + u_2^2 + u_3^2} \approx 0.53 \text{ kN}$$

with estimated expanded uncertainty $U = 2u_c \approx 1.07$ kN using a coverage factor ($k = 2$). The measured capacity increments exceed the estimated combined standard uncertainty, $WP_0 \rightarrow WP_2 = +1.95$ kN $(3.7 \times u_c)$ and $WP_0 \rightarrow WP_4 = +2.81$ kN $(5.3 \times u_c)$, without establishing statistical significance or repeatability.

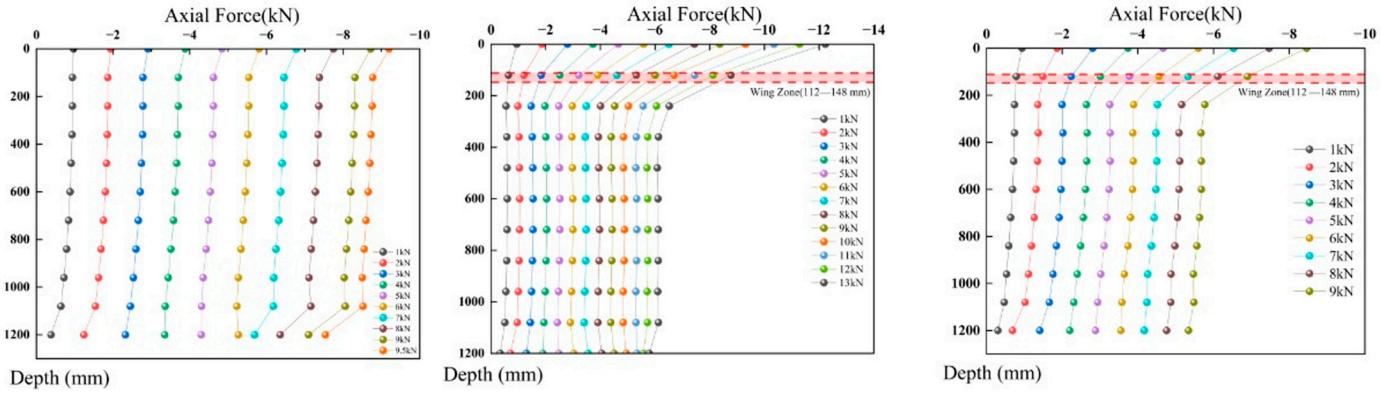
Within-test gauge agreement indicates loading symmetry but does not establish statistical repeatability across independently reconstituted soil beds. The soil bed variability

term was instead estimated from the observation that a single, invariant set of calibrated soil-constitutive parameters reproduced all three measured load–settlement curves within ≤6% error (Table 5). While leave-one-out cross-validation and numerical parametric evaluations provide complementary predictive verification, they do not substitute for physical replicate testing; this constraint is explicitly acknowledged as a boundary limitation of the present experimental program.

3.4. Load Transfer Mechanism of Winged Piles

3.4.1. Axial Force Diagram

Under axial force distribution, $N(z)$, normal stresses were extracted via free-body cuts at 120 mm intervals along the pile shaft and integrated across the cross-section. Figure 11 illustrates the resulting $N(z)$ profiles for all three model piles at successive load levels. Because these distributions are derived from the validated models, they precisely reflect the conditions under which each physical laboratory test was reproduced. For the plain pile (WP0), axial force decreases smoothly and linearly with depth. Successive load increments shift the profile in a nearly parallel manner, but the overall gradient remains gentle. Because the bulk of the head load reaches the toe even at maximum loading, WP0 clearly behaves as an end-bearing-dominated pile in loose Malan loess, restricted by low lateral effective stress. The winged piles, however, trigger a distinct two-region response. In the upper wing zone (the top 240 mm), the force profiles drop sharply: at peak load, WP2 sheds roughly 2.8 kN (one-third of the head load), while WP4 sheds 3.9 kN (nearly half). Below the wings, the curves flatten significantly, showing that very little additional load transfers via friction along the remaining length. Two behavioral traits are particularly noteworthy here. First, the steep force gradient in the wing zone is present from the very earliest load increments and simply steepens as the load grows. This confirms that the wings engage the soil immediately and remain continuously active, rather than mobilizing only near ultimate failure. Second, the overall geometry of the profile, a sharp initial drop followed by a gradual lower gradient, remains remarkably consistent across all load steps, proving that this load-sharing mechanism is established early and remains highly stable up to failure.



(**a**) WP0 (**b**) WP2 (**c**) WP4

Figure 11. Axial force distribution diagram for model piles.

3.4.2. Hyperbolic Interface Model and Component Calibration

Hyperbolic functions are the standard method for characterizing how pile foundations transfer load, effectively mapping the non-linear relationship between interface stress and relative displacement. This concept was first used by Seed and Reese [53] and adopted by several researchers for broader soil–structure interaction inferences [54–56].

In this study, a unified hyperbolic model across all soil–pile interface components was set out as

$$q = \frac{w}{a + b \cdot w} \quad (1)$$

where w is the relative displacement and q is the corresponding interface stress (shaft shear stress τ, wing pressure q_w, or base pressure q_b). The mathematical parameters a and b govern the curve: $k_{ini} = 1/a$ defines the initial stiffness, and $q_{ult} = 1/b$ dictates the asymptotic ultimate stress. We established a validated baseline by first calibrating this model against the plain monopile shaft response, and then extended it to evaluate the individual wing and base components of the winged piles.

Monopile $t - z$ Calibration (Validation Baseline)

A validation baseline was established by calibrating the hyperbolic model against the shaft friction–settlement ($t - z$) response of the plain monopile (WP0) across multiple depths (z = 120, 240, 360, 480, 600, and 720 mm). At each elevation, shear stress (τ) was extracted from the interfacial CSHEAR distribution, and relative displacement (w) was defined by the incremental settlement. These variables were transformed ($X = w$, $Y = w/\tau$) to perform a linear regression of the form $Y = a + b \cdot w$. Every shaft regression achieved $R^2 > 0.98$ (Table 6); the tip (Table 7) and wing bearing (Table 8) R^2 values range from 0.933 to 0.999. The two lowest values (0.934 for WP2 tip, Table 7; 0.933 for WP4 wing bearing, Table 8) occur for the components that mobilize over the shortest displacement ranges; all shaft fits exceed 0.98. The hyperbolic model therefore captures the nonlinear mobilization of interface resistance in loess across all components, proving that the hyperbolic model effectively captures the nonlinear mobilization of shaft friction in loess.

Table 6. Hyperbolic $t - z$ parameters for the monopile shaft at multiple depths.

Depth z (mm)	a (mm/kPa)	b (kPa^{-1})	$k_{ini} = 1/a$ (kPa/mm)	$\tau_{ult} = 1/b$ (kPa)	R^2
120	2.58	0.93	0.39	1.07	98.26%
240	1.02	0.84	0.98	1.19	99.67%
360	0.28	0.74	3.57	1.35	99.97%
480	0.20	0.65	4.92	1.53	99.98%
600	0.07	0.60	14.83	1.68	99.99%
720	0.014	0.53	72.03	1.87	99.99%
840	−0.43	0.56	−2.33 [a]	1.79	99.77%
960	−0.09	0.49	−11.27 [a]	2.06	98.75%

Note: [a] Negative intercept in the unconstrained fit; k_{ini} is discarded at these depths while τ_{ult} is retained, as justified in Section 3.4.2 under the heading "Monopile $t - z$ Calibration (Validation Baseline)".

Table 7. Hyperbolic $q - w$ parameters for pile tip bearing.

Pile Model	a (mm/kPa)	b (kPa^{-1})	$k_{ini} = 1/a$ (kPa/mm)	$\tau_{ult} = 1/b$ (kPa)	R^2
WP0	0.00663	0.00143	150.89	700.12	0.984
WP2	0.00521	0.00174	191.96	575.34	0.934
WP4	0.00626	0.00163	159.83	611.83	0.989

Table 8. Hyperbolic $q - w$ parameters for wing–soil bearing.

Wing Pile Model	a (mm/kPa)	b (kPa^{-1})	$k_{ini} = 1/a$ (kPa/mm)	$\tau_{ult} = 1/b$ (kPa)	R^2
WP2	0.00259	0.00105	386.77	949.56	0.983
WP4	0.00394	0.00095	253.79	1052.95	0.933

Across shallow and intermediate depths ($z \leq 720$ mm), the interface response conforms closely to classical mobilization behavior, yielding a physically consistent positive

initial shear stiffness ($k_{\text{ini}} = 1/a > 0$). At deeper elevations (z = 840 mm and 960 mm), however, linear regression of the transformed data yields a negative intercept ($a < 0$), resulting in an unphysical negative initial stiffness. This discrepancy arises because interface shear resistance at these depths mobilizes rapidly within extremely small relative displacements (Figure 12), and subsequently exhibits subtle strain-softening following a localized peak feature that a strictly monotonic hyperbolic formulation cannot capture. Inspection of the raw FE stress–displacement data points at these depths (Figure 12) confirms that the negative intercept reflects genuine strain softening in the first load increment, not a mathematical artifact of the regression. While this negative intercept represents a recognized modeling artifact of the standard hyperbolic law at these two depths, we acknowledge this as a limitation of the adopted formulation; it does not compromise the validity of the results. First, the asymptotic ultimate shear strength ($\tau_{\text{ult}} = 1/b$) is governed by the slope (b) of the linearized hyperbolic transformation ($s/\tau = a + bs$) at larger relative displacements, rendering the strength parameter essentially insensitive to intercept perturbations or its algebraic sign. Second, the derived ultimate shear stresses at z = 840 mm and 960 mm (1.79 kPa and 2.06 kPa, respectively; Table 6) smoothly continue the systematic, depth-dependent increase established across shallower elevations, corroborating their physical consistency. Consequently, the anomalous k_{ini} values at these two depths were discarded, while the corresponding τ_{ult} values (1.79 kPa and 2.06 kPa) were retained. This partial retention is justified because τ_{ult} is governed by the slope of the linearized hyperbolic transformation at larger displacements and is insensitive to intercept perturbations or its algebraic sign; only the non-physical initial stiffness is excluded from subsequent capacity calculations. Formulating an interface constitutive relationship capable of capturing post-peak strain softening at deeper boundaries is identified as an area for future refinement. The fitted parameters demonstrate a systematic, depth-dependent increase in ultimate shaft friction ($\tau_{ult} = 1/b$), rising from approximately 1.07 kPa at z = 120 mm to 2.06 kPa at z = 960 mm (Table 6). This trend perfectly reflects the β-method for $c - \varphi$ soils, where greater overburden depth increases lateral effective stress ($\sigma'_h = K_0 \gamma z$), thereby boosting the Mohr–Coulomb interface shear strength ($\tau_s = c' + \sigma'_n tan\delta$). The initial stiffness also increases with depth, reflecting the greater soil confinement and resistance to initial shear displacement at deeper elevations.

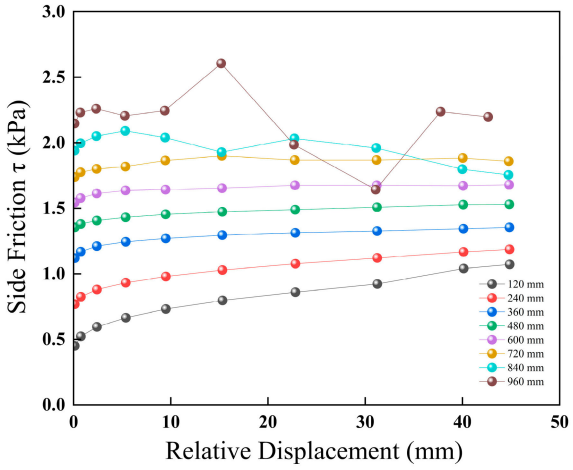


Figure 12. $\tau - z$ curves for the monopile (WP0).

Pile Tip Radial Pressure $q - w$ Characterization

To evaluate pile tip resistance, the radial CPRESS profile, $q(r)$, at the pile base was axisymmetrically integrated, and the resulting average base pressure was fitted against

settlement using a hyperbolic function. The average base pressure was calculated via numerical integration using the trapezoidal rule,

$$q_{b,avg} = \frac{2\pi \int_0^R q(r) \cdot r\, dr}{\pi R^2} \approx \frac{2\pi \sum_i \frac{q_i r_i + q_{i+1} r_{i+1}}{2} \Delta r_i}{\pi R^2} \quad (2)$$

The derived base pressure–settlement data were then fitted to the hyperbolic equation $q = w/(a + bw)$. Table 7 summarizes these final fitted parameters for each pile configuration and Figure 13 compares the pile base-soil bearing pressure of three model piles.

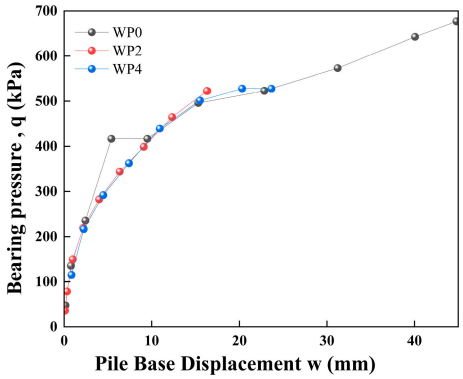
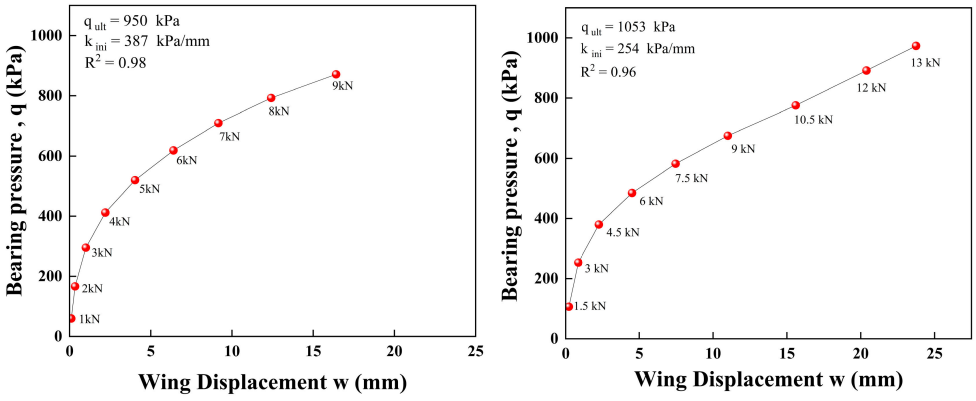


Figure 13. Comparison of pile base-soil bearing pressure displacement (q-w) curves for three model piles.

Wing–Soil Bearing $q - w$ Characterization

While hyperbolic models are widely validated for standard pile shaft ($t - z$) and tip (Q–z) load transfer [54–56], their application to wing–soil interfaces has not been previously documented. This study addresses that gap by extending the hyperbolic formulation to the wing's bottom face, modeling it as a planar soil–structure interface under normal compression (Figure 14). This approach is rooted in the physical basis that wing–soil contact obeys the same asymptotic pressure–settlement laws governing the tip and shaft, defined by an initial stiffness ($k_{ini} = 1/a$) and an ultimate bearing pressure ($q_{ult} = 1/b$).



(a) WP2 (b) WP4

Figure 14. Wing–soil bearing pressure–displacement ($q - w$) curves for (**a**) the WP2 2-wing pile and (**b**) the WP4 4-wing pile, showing the hyperbolic mobilization of contact pressure at the wing bottom face.

Wing–soil bearing pressures were obtained by extracting path-averaged CPRESS distributions along the wing centerline across load stages of 1–9 kN (WP2) and 1.5–13 kN (WP4). The hyperbolic model was then fitted to the corresponding $q - w$ data for each configuration, as per Table 8.

3.4.3. Decomposition of Vertical Bearing Capacity

The total vertical compressive capacity of the winged pile, Q_u, is decomposed into three primary components: pile tip resistance R_b, the end-bearing resistance R_w, and the side resistance Q_s, which encompasses both the pile shaft friction and the wing side friction. The equilibrium equation is expressed as

$$Q_u = R_b + R_w + Q_s \quad (3)$$

where Q_s denotes the total side resistance, comprising both cylindrical pile shaft friction and wing-side interface shear. The base resistance R_b and wing bearing resistance R_w are evaluated through the direct surface integration of normal contact pressures (CPRESS). Total side resistance Q_s is then determined by residual deduction from global equilibrium [Equation (4): $Q_s = Q_u - R_b - R_w$]. For independent verification, wing-side shear was directly quantified via the integration of tangential contact stresses (CSHEAR1) over the vertical wing surfaces (web faces and flange edges, 2774 mm^2 engaged area), yielding 0.009 kN; shaft friction follows as the remainder of Q_s. Component-wise equilibrium closure ($R_b + R_w + Q_s$ versus total reaction force) closed within 0.3%.

$$Q_s = Q_u - R_b - R_w \quad (4)$$

All components were evaluated at the standard settlement criterion of $s = 0.1d = 10$ mm, consistent with conventional pile failure criteria [27]. The load–settlement data for each pile configuration (WP0, monopile; WP2, two-wing pile; WP4, four-wing pile) were extracted from the validated Abaqus FEM models. The pile tip resistance was determined by axisymmetric integration of the contact pressure distribution $q(r)$ extracted from the soil–pile interface at the pile base. The normal stress components (R_b and R_w) and the wing-side shear subset are obtained by direct integration; Q_s is the residual side resistance from Equation (4). Closure was verified within 0.3%. For a circular pile tip of radius (R), the vertical reaction force for pile tips is:

$$R_b = 2\pi \int_0^R q(r).rdr \quad (5)$$

The radial CPRESS profile was discretized into annular segments, and the integral was evaluated using the trapezoidal rule, as described in Equation (5), where q_i is the contact pressure at radial position r_i , and $\Delta r_i = r_{i+1} - r_i$. This approach inherently accounts for the annular area distribution in axisymmetric problems and avoids the overestimation associated with arithmetic averaging. For wing-bearing resistance (R_w), the vertical force of each wing was determined by integrating the path averaged contact pressure along the wing projection. The bottom face of the wing was treated as a rectangular bearing surface of width $W = 14$ mm and projection length $B = 45$ mm. The wing reaction force is

$$R_w = N_w \cdot W \int_0^B q(x)dx \quad (6)$$

The CPRESS paths were extracted from the wing–soil interface at $s = 0.1d$ for WP2 and WP4. The monopile (WP0) has $R_w = 0$ by definition. Table 9 presents the decomposed load components and their respective shares for the three pile configurations at $s = 0.1d = 10$ mm.

Table 9. Ultimate compressive capacity, resistance components, and their percentage contributions for the three model piles at a pile-head settlement of 10 mm ($s = 0.1d$).

Pile	Q_u (kN)	Q_s (kN)	R_b (kN)	R_w (kN)	Side (%)	Base (%)	Wing (%)
WP0	5.08	2.05	3.03	0	40.35	59.65	0
WP2	7.27	3.42	2.97	0.88	47.04	40.85	12.10
WP4	8.59	4.11	2.85	1.63	47.85	33.18	18.98

Note: Q_s, total side resistance. The wing-side contribution (0.009 kN) was obtained by direct sub-area integration of CSHEAR1 over the wing vertical faces; the shaft friction is the remainder of the combined vertical surface CSHEAR1 integration. All normal stress components (R_b, R_w) are direct CPRESS integrations.

The internal composition of the side resistance (Q_s) was verified through direct surface integration of the contact shear tractions in the validated WP4 finite element model. Integrating the tangential contact stresses across the vertical faces of the exposed wings (comprising all vertical faces of the I-section wing both lateral faces of the web and all end faces (edges) of the top and bottom flanges in contact with soil, representing an engaged surface area of 2774 mm^2) yields a total wing-side shear force of 0.009 kN. This corresponds to an average interface shear stress of 3.3 kPa, which is of the same order of magnitude as the average cylindrical shaft shear stress (8.3 kPa). Hence, the negligible magnitude of the wing-side shear force is primarily a consequence of its limited surface area (approximately 2% of the engaged shaft surface area) rather than any disparity in interface friction mobilization. Wing-side friction accounts for only $\approx$ 0.2% of the total side resistance (Q_s = 4.20 kN) (Table 9), confirming that the residual side quantity defined in Equation (4) is, for practical engineering purposes, almost entirely governed by cylindrical shaft skin friction. Global equilibrium was verified independently by extracting the resultant reaction force at the loaded reference point (8681.9 N at $s = 0.1d$ = 10 mm), which matched the total vertical compressive capacity (Q_u). Component-wise equilibrium closure was verified; the sum of R_b, R_w, and Q_s (shaft friction plus vertical wing-side shear) closed against the applied load within 0.3%, confirming that all contact forces were fully accounted for across the interface surfaces. Furthermore, while the solver writes contact field output exclusively for actively tracking slave nodes, the global force balance confirms that the remainder of Q_s is transferred through active shaft contact pairs that were excluded from the selective output database during the element deactivation and reactivation installation procedure. This post-processing output artifact does not compromise the validity of the load decomposition, as even under a conservative full-area recovery assumption, the wing-side shear contribution remains strictly below 1% of the total side resistance. Figure 15 shows a visual representation of the load transfer decomposition of three model piles at the ultimate state.

The load transfer behavior observed in this study follows the fundamental mechanism established for piles in *c*-φ soils, wherein shaft friction mobilizes at a relative displacement of 5–10 mm while end bearing requires a tip movement of 10–25% of the pile diameter to reach full capacity [57]; consequently, at the standard failure criterion of $s = 0.1d$ (10 mm), the side resistance is nearly fully mobilized, whereas the tip resistance remains partially developed. Unlike under-reamed piles in saturated clay—where enlarged bulbs near the pile tip compress the surrounding soil and reduce shaft adhesion [58]—the wing plates in this study are positioned along the pile shaft and act as lateral displacement elements that compact the metastable loess structure, thereby increasing the lateral effective stress and enhancing the Mohr–Coulomb interface shear strength ($\tau_s = c' + \sigma'_h tan\delta$) along the pile shaft.

The von Mises stress field in the surrounding soil (Figure 16) highlights this phenomenon even more sharply. Beneath the plain pile, a severe high-stress zone concentrates directly around the base perimeter. In stark contrast, the soil beneath the winged piles remains almost entirely at low stress. This occurs because the wings have already intercepted

and transferred a massive portion of the load into shallower soil layers. Ultimately, the wings do more than just redistribute the load at the ultimate state—they fundamentally shift the entire center of load transfer upward, safely away from the pile toe.

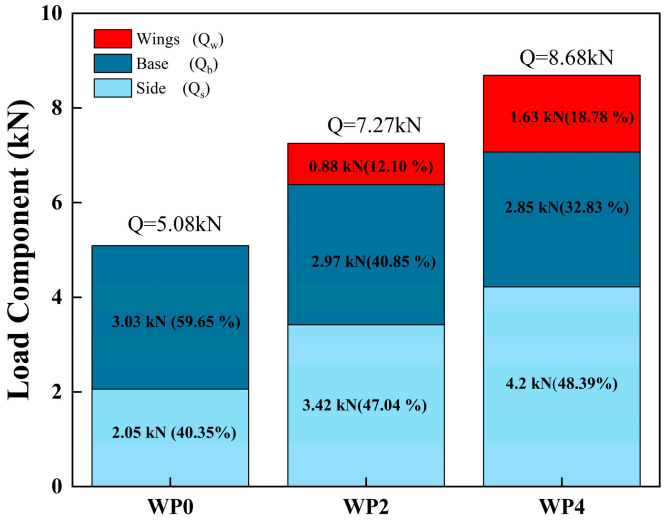
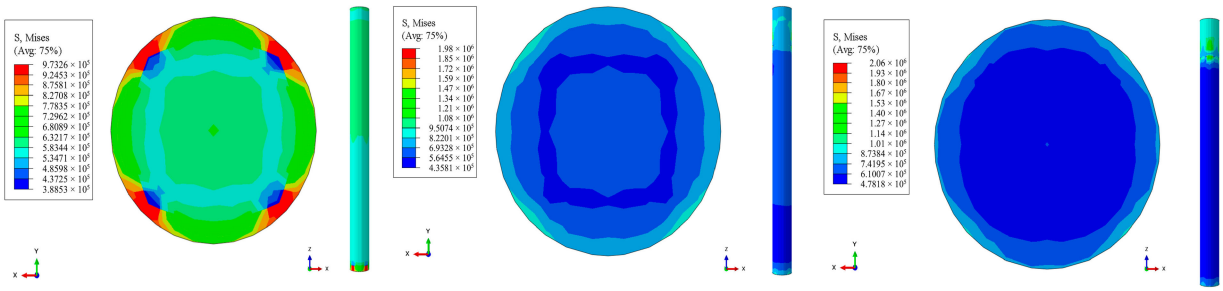


Figure 15. Comparison of side, base, and wing resistance in the WP0, WP2, and WP4 model piles at a pile-head settlement of 10 mm. $(s = 0.1d)$.



(a) WP0 (b) WP2 (c) WP4

Figure 16. Von Mises stress field in the soil surrounding the pile base at the ultimate state $(s = 0.1d = 10\ \text{mm})$ obtained from the baseline finite element models.

3.5. Parametric Study of Wing Geometry

To explore the influence of individual design and soil variables, a one-factor-at-a-time parametric study was conducted using the validated four-wing baseline model (WP4). The baseline configuration utilized a wing height (h) of 36 mm, a wing projection (B) of 45 mm, and a pile length (L) of 1200 mm, set within a loess soil defined by a cohesion (c) of 15.5 kPa and an elastic modulus (E_s) of 20 MPa. From this established baseline, fifteen additional cases were simulated by varying a single parameter while holding all others constant. The isolated variables included the number of wings $(n = 0,\ 2)$, wing projection $(B = 30,\ 60,\ 70\ \text{mm})$, wing height $(h = 25,\ 50\ \text{mm})$, pile length $(L = 800,\ 1600\ \text{mm})$, soil cohesion $(c = 10,\ 25\ \text{kPa})$, soil elastic modulus $(E_s = 10,\ 25\ \text{MPa})$ and wing embedment depth $(h_w = 80,\ 180\ \text{mm})$.

Every analysis was executed under displacement-controlled loading. To ensure a consistent and practical comparison, the compressive capacity for each scenario was evaluated at the standard reference settlement of $s = 0.1d$ (10 mm), as previously defined in Section 3.2. The resulting load–displacement curves for all variations are illustrated in Figure 17, and their corresponding capacities at the 10 mm threshold are detailed in Table 10. Geometric modifications reveal that the wing number (n) has the strongest influence on load-bearing

behavior (Figure 17g). Capacity increases from 5.08 kN($n = 0$) to 7.27 kN ($n = 2$) and 8.68 kN ($n = 4$), producing improvement factors of 1.43 and 1.71. Wing projection (B) offers an almost linear benefit (Figure 17a); increasing the projection from 30 to 70 mm boosts capacity by 28.8% because it expands the effective bearing area by mobilizing the soil. Wing height (h), however, has a negligible effect ($<\pm 2.2$) (Figure 17b), proving that resistance depends on the wing's horizontal projection, not its vertical profile.

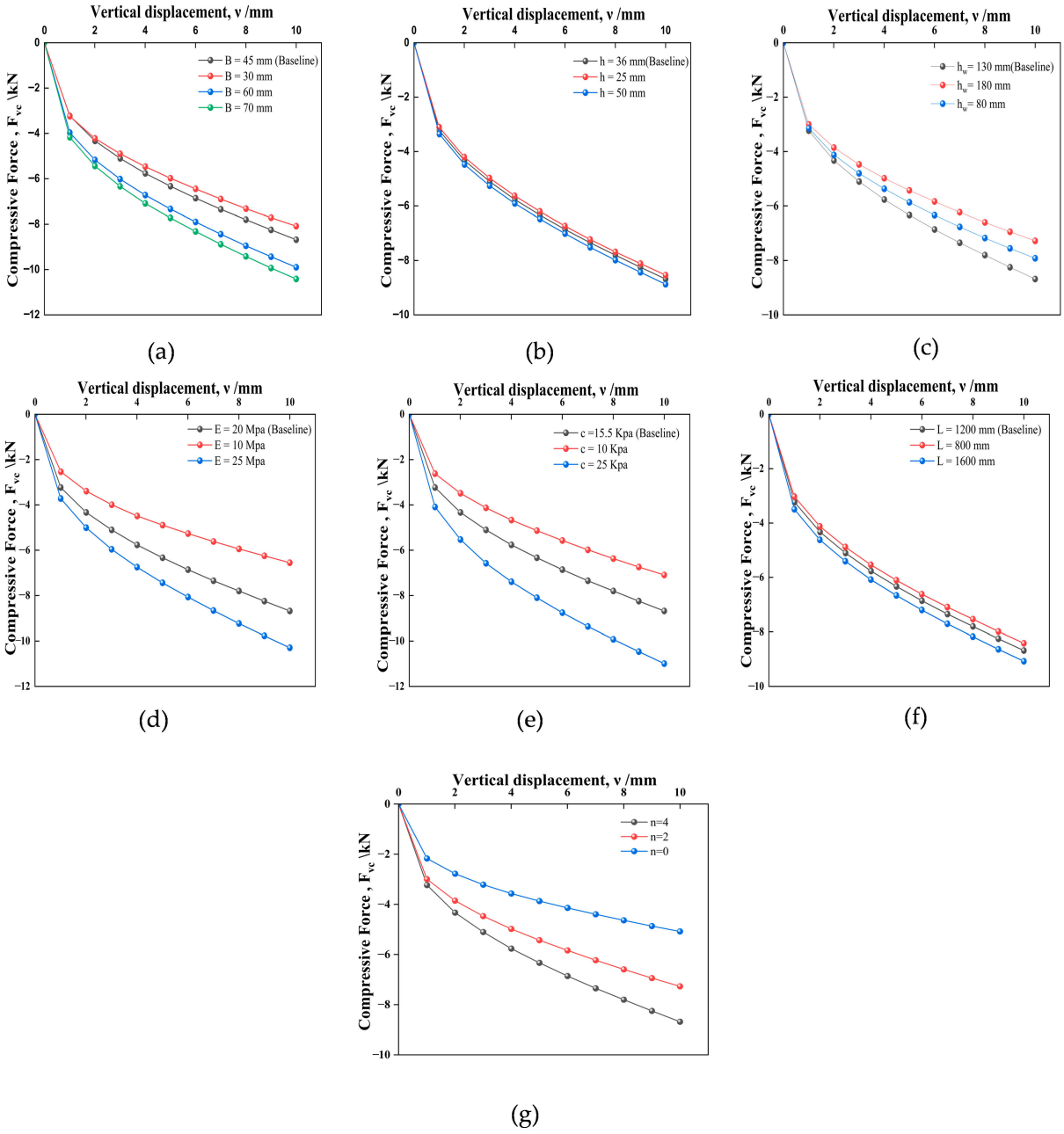


Figure 17. Compressive force vs. vertical displacement curve for different parameters of WP4 at $s = 0.1d$ (10 mm). The panels show the effects of (**a**) wing projection, (**b**) wing height, (**c**) wing embedment depth, (**d**) soil elastic modulus, (**e**) soil cohesion, (**f**) pile length, and (**g**) number of wings on the load–settlement response.

Table 10. FE-computed compressive capacity of the 16 calibration cases at $s = 0.1d = 10$ mm, with leave-one-out cross-validated (LOOCV) predictions.

S. N	Parameter Varied	Case	Value	Q at s = 10 mm (kN)	Q Predicted, LOOCV (KN)	Error (%)
1	Baseline	WP4	—	8.68	8.65	−0.33
2	Wing number n	WP0	0	5.08	5.41	+6.54 [s]
3	Wing number n	WP2	2	7.27	7.26	−0.19
4	Wing projection B	WP4-B30	30 mm	8.09	7.46	−7.85
5	Wing projection B	WP4-B60	60 mm	9.90	9.60	−3.07
6	Wing projection B	WP4-B70	70 mm	10.41	10.16	−2.41
7	Wing height h	WP4-H25	25 mm	8.54	8.47	−0.83
8	Wing height h	WP4-H50	50 mm	8.87	8.76	−1.22
9	Pile length L	WP4-PL800	800 mm	8.42	8.09	−3.95
10	Pile length L	WP4-PL1600	1600 mm	9.07	8.86	−2.36
11	Cohesion c	WP4-C10	10 kPa	7.09	6.99	−1.40
12	Cohesion c	WP4-C25	25 kPa	10.99	10.89	−0.94
13	Elastic modulus (E_s)	WP4-E10	10 MPa	6.55	6.30	−3.82
14	Elastic modulus (E_s)	WP4-E25	25 MPa	10.30	9.36	−9.15
15	Wing Embedment (h_w)	WP4-ED80	80 mm	7.92	8.72	+10.09 [s]
16	Wing Embedment (h_w)	WP4-ED180	180 mm	7.28	8.76	+20.34 [s]

Note. Baseline WP4: $h = 36$ mm, $h_w = 130$ mm, $B = 45$ mm, $L = 1200$ mm, $c = 15.5$ kPa, $E_s = 20$ MPa, $n = 4$. Q Predicted LOOCV (kN) is the blind prediction of each case by an equation re-fitted without that case (Section 4.3). [s] WP0, ED80 and ED180 are the three boundary folds: WP0 is the sole $n = 0$ configuration, which identifies the monopile/wing decomposition; ED80/ED180 are embedment-variation cases whose effects are not explicitly represented in the equation (Section 3.5). Excluding these three folds, the core-case LOOCV MAPE is 2.89%.

As shown in Figure 17c, the wing embedment depth (h_w) exhibits a distinctly non-monotonic influence on capacity. For the investigated reduced-scale baseline configuration under the specified soil and geometric conditions, the highest bearing capacity was obtained at the baseline depth ($h_w = 130$ mm, $h_w/d = 1.3$). Moving the wings shallower (80 mm, $h_w/d = 0.8$) or deeper (180 mm, $h_w/d = 1.8 = 1.8$) reduces overall capacity by 8.8% and 16.1%, respectively. Because the corresponding load–settlement curves match closely at small settlements before ultimately diverging, embedment depth clearly governs the progressive mobilization of wing resistance rather than the foundation's initial stiffness.

Two distinct mechanical behaviors explain these losses. At shallow depths, limited soil cover (only $0.8d$) causes the wing bearing mechanism to interact with the free surface, prematurely yielding like a shallow plate anchor. At greater depths, the extended upper shaft transfers more load into the adjacent soil, pulling it downward. This drag-down interference reduces the relative pile–soil displacement at the wings, thereby limiting their mobilized resistance. This optimum is specific to the investigated reduced-scale baseline configuration and working conditions ($c = 15.5$ kPa, $E_s = 20$ MPa, $d = 100$ mm, dry remolded Malan loess). However, since capacity fluctuates by a maximum of 16.1% across this operational range, the embedment effect in this study is secondary to those effects of wing count and projection width. The unified capacity expression developed in Section 4 is referenced to the observed baseline embedment ($h_w/d = 1.3$). The interval $h_w/d \in [0.8, 1.8]$ records the examined embedment range and is not a range of validated equation accuracy. Embedment effects require case-specific numerical verification. The formula lacks an explicit embedment term and cannot directly predict capacity losses away from the observed optimum; the −8.8% and −16.1% deviations at $0.8d$ and $1.8d$ are documented penalties, not auto-predicted by the equation. For the particular full-scale numerical series in Section 4.4, the computed capacity varies by less than ±0.7% across $h_w/d = 0.5 - 2.0$.

Soil parameters similarly dominate pile performance Figure 17d,e. Modifying soil cohesion (c) from 15.5 kPa down to 10 kPa or up to 25 kPa shifts the capacity by −18.3% and

+26.6%, respectively (averaging ~0.27 kN/kPa). The elastic modulus (E_s) exerts a similar proportional influence (−24.5% at 10 MPa; +18.6% at 25 MPa) because a stiffer soil skeleton resists higher loads at identical settlements. However, modifying pile length (L) between 800 and 1600 mm altered capacity by only ±3–4.5% (Figure 17f). This confirms that winged pile capacity is dominated by wings and a shallow shaft rather than the depth of the pile embedment. It should be noted that the 16-case parametric matrix varies one parameter at a time from a common baseline. This design isolates main effects but does not systematically test parameter interactions (e.g., between wing projection and soil stiffness). The fitted power-law model implicitly assumes multiplicative separability, which the present database cannot rigorously verify beyond the calibrated domain.

3.6. Scale Similitude and Experimental Uncertainty

The reduced-scale model tests follow geometric and material similitude considerations for the prototype winged pile: the governing dimensionless geometric ratios (B/d, h/d, L/d, and h_w/d) define comparisons between the model and prototype scales, while the reconstituted loess (c = 15.5 kPa, E_s = 20 MPa, φ = 20°) represents the dry, remolded soil conditions adopted in the numerical comparisons. Accordingly, the load response is evaluated at the normalized displacement threshold of $s = 0.1d$, which eliminates settlement-scale ambiguity. A well-known limitation of 1 g physical modeling is the gravity–stress mismatch. At the physical model scale, the gravity–stress ratio $\rho g d/E_s$ is 8–10 times smaller in the model (d = 100 mm) than at prototype scale (d = 800–1000 mm), constituting the fundamental 1 g scaling limit. Rather than neglecting this stress under-representation, this study addresses it explicitly through dimensional analysis. Section 4.1 identifies π_8 as an independent dimensionless parameter; Section 4.4 introduces a correction calibrated from one full-scale numerical monopile reference and examines the resulting predictions against additional prototype-scale finite-element cases.

The experimental program comprised single benchmark tests on three configurations (n = 0, 2, 4). Because large-chamber model tests require extensive soil preparation, placement, and uniform compaction, replicate testing was not practically feasible; consequently, the experimental results serve as physical verification benchmarks for the finite element model rather than a statistical sample. The numerical analyses provide sensitivity information but do not establish repeatability across independently prepared soil beds. Specifically, the 16-case parametric investigation (Section 3.5) and leave-one-out cross-validation (Section 4.3) provide sensitivity and regression prediction checks within the investigated numerical cases, while the physical test curves provide the experimental anchor. The physical tests provide benchmark comparisons, while repeatability remains unquantified in the absence of independent replicate tests.

An estimated engineering uncertainty budget following GUM principles assumes independence among three sources: (i) load discretization (rectangular distribution over ±0.5 kN, $u_1 = 0.5/\sqrt{3} \approx 0.289$ kN); (ii) displacement measurement (rectangular distribution over ±0.18 mm converted via secant stiffness, $u_2 \approx 0.18$ kN); and (iii) soil bed preparation variability (inferred from finite-element validation scatter rather than independent replicate experiments, ≤ 6%, $u_3 \approx 0.41$ kN). These yield a combined standard uncertainty of $u_c = \sqrt{u_1^2 + u_2^2 + u_3^2} \approx 0.53$ kN and an expanded uncertainty of $U \approx 1.07$ kN at a coverage factor of $k = 2$ (≈95% nominal coverage under a normal approximation). This is an estimated engineering uncertainty budget, not a statistically established 95% confidence interval for experimental repeatability. Independent replicate experiments were not performed, so statistical repeatability cannot be established.

The load–settlement response was captured under load-controlled conditions using uniform increments of 1 kN. At each loading stage, the applied actuator force was recorded

via an in-line load cell, while displacements were monitored using three independent instruments: a draw-wire displacement transducer and two precision dial gauges (resolution 0.01 mm) mounted symmetrically on diametrically opposite sides of the pile head. Final displacement readings were logged once settlement satisfied standard stabilization criteria under sustained loading. The capacity for each configuration was subsequently extracted from the continuous load–displacement curve at the normalized settlement threshold of $s = 0.1d$. Consequently, the discrete load-step magnitude governs the point density along the response curve rather than introducing systematic error to the capacity determination. The potential uncertainty associated with load discretization is bounded within a small fraction of a single increment and remains systematically uniform across all three configurations. These steps of parameter loading (1kN), gauge resolution (0.01 mm), observed maximum gauge divergence (0.36 mm) and target dry density (1.75 g/cm^3) were verified against the original laboratory logbooks and soil preparation sheets.

Each experiment was conducted in a freshly reconstituted soil bed, with the entire soil volume excavated, reconditioned, and compacted between tests following a standardized protocol that held compaction effort and target density constant. While replicate testing was not practically feasible given the substantial effort required for complete bed replacement, the available information supports an engineering uncertainty estimate rather than a statistical estimate of between-bed repeatability. First, a single, invariant set of soil-constitutive parameters ($c = 15.5$ kPa, $E_s = 20$ MPa, $\varphi = 20°$) reproduced the measured response across all three foundation configurations to within 6% error (Table 5), which provides validation scatter for the estimated soil bed variability term but does not independently measure between-bed variability. Second, within each test, the two independent dial gauges mounted on opposite sides of the shaft agreed within 0.36 mm throughout loading ($\leq$3.6% of the $s = 0.1d$ criterion displacement), indicating within-test gauge agreement and symmetrical load transfer. It is emphasized that this 0.36 mm agreement characterizes within-test measurement precision only; it does not demonstrate between-batch repeatability, which would require multiple specimens tested in independently prepared soil beds. Likewise, leave-one-out cross-validation and finite-element parametric studies evaluate regression generalization and numerical fidelity, respectively, but they cannot replace the statistical repeatability analysis of physical tests. Finally, the measured capacity gains from WP0 to WP2 and WP4 (+1.95 kN and +2.81 kN, representing +36% and +52% increases, respectively) exceed the estimated combined standard uncertainty ($u_c \approx 0.53$ kN) by factors of 3.7 and 5.3, respectively, indicating differences larger than this engineering estimate without establishing statistical significance or experimental repeatability.

4. Unified Ultimate Capacity Expression via Buckingham π Theorem

4.1. Theoretical Framework

The Buckingham theorem [29] states that if a physical phenomenon involves n dimensional variables and m fundamental dimensions, the phenomenon can be described by n-m independent dimensionless π terms. For the ultimate bearing capacity of a wing pile, $n = 15$ physical quantities were identified (Table 11), with 14 input variables spanning geometry, material properties, and soil state, while soil unit weight is excluded because it is derived from mass density and gravitational acceleration g via $\gamma = \rho g$; g is included explicitly to ensure dimensional independence and to capture self-weight stresses. The fundamental dimensions are (M, L, T). Dimensional independence was verified by the non-zero determinant of the exponent matrix (Equation (7)),

$$\begin{vmatrix} 0 & 1 & 0 \\ 1 & -1 & -2 \\ 1 & -3 & 0 \end{vmatrix} = -2 \neq 0 \quad (7)$$

Table 11. Parameter dimension table.

No.	Symbol	Description	Dimension (MLT)
1	Q_u	Ultimate bearing capacity	MLT^{-2}
2	d	Pile shaft diameter	L
3	B	Wing projection (radial)	L
4	h	Wing height (vertical height of the I-section wing)	L
5	b_f	Wing flange width	L
6	h_w	Wing embedment depth	L
7	L	Pile embedment length	L
8	E_p	Pile elastic modulus	$ML^{-1}T^{-2}$
9	E_s	Soil elastic modulus	$ML^{-1}T^{-2}$
10	c	Soil cohesion	$ML^{-1}T^{-2}$
11	φ	Soil friction angle	$M^0L^0T^0$
12	ρ	Soil mass density	ML^{-3}
13	g	Gravitational acceleration	LT^{-2}
14	n	Number of wings	$M^0L^0T^0$
15	ω	Soil moisture content	$M^0L^0T^0$

Note: (a) In the wing-projection cases, only the exposed projection B was varied (30, 60, 70 mm); the embedded length B_{emb} = 20 mm was held constant, so $B_w = B + B_{emb}$. (b) Soil unit weight γ is related to mass density ρ and gravitational acceleration g by $\gamma = \rho g$. Because γ is a derived quantity, it is excluded from the independent variable count; g is included explicitly as row 13 to ensure dimensional independence and to capture self-weight stress effects.

For $n - m = 15 - 3 = 12$, the dimensional terms that can be assembled as

$$F(\pi_1, \pi_2, \pi_3, \pi_4, \pi_5, \pi_6, \pi_7, \pi_8, \pi_9, \pi_{10}, \pi_{11}, \pi_{12}) = 0 \quad (8)$$

The dimensionless π terms are derived by enforcing dimensional homogeneity,

$$[\pi_i] = M^0 L^0 T^0 :$$

$$\pi_1 = \frac{Q_u}{E_s d^2} \quad (9)$$

$$\pi_2 = \frac{B}{d} \quad (10)$$

$$\pi_3 = \frac{h}{d} \quad (11)$$

$$\pi_4 = \frac{b_f}{d} \quad (12)$$

$$\pi_5 = \frac{L}{d} \quad (13)$$

$$\pi_6 = \frac{E_p}{E_s} \quad (14)$$

$$\pi_7 = \frac{c}{E_s} \quad (15)$$

$$\pi_8 = \frac{\rho g d}{E_s} \quad (16)$$

$$\pi_9 = \varphi \quad (17)$$

$$\pi_{10} = n \tag{18}$$

$$\pi_{11} = \omega \tag{19}$$

$$\pi_{12} = \frac{h_w}{d} \tag{20}$$

Of the twelve groups, φ (= 20°), ω, and b_f/d (= 0.14) were held constant in the parametric study, whereas $\rho g d/E_s$ (= 8.58×10^{-5} at the model-scale baseline) varied through E_s; only the fixed geometric and material groups are absorbed into the constants C_{mono} and C_{wing}. The gravity–stress ratio remains explicit in the normalized correction factor G defined below, rather than being absorbed into those constants. The embedment group $\pi_{12} = h_w/d$, however, exhibits a non-monotonic influence with an optimum at $h_w/d = 1.3$ (Section 3.5), and cannot be represented by any single power law term; its optimum is retained as an observation specific to the investigated reduced-scale baseline, and the equation contains no explicit embedment term. The interval $0.8 \leq h_w/d \leq 1.8$ denotes examined embedment ratios and does not establish predictive accuracy throughout that interval.

The functional relationship is expressed as a power law product,

$$\frac{Q_u}{E_s d^2} = C.\left(\frac{B}{d}\right)^{a_1}\left(\frac{h}{d}\right)^{a_2}\left(\frac{b_f}{d}\right)^{a_3}\left(\frac{L}{d}\right)^{a_4}\left(\frac{E_p}{E_s}\right)^{a_5}\left(\frac{c}{E_s}\right)^{a_6}\left(\frac{\rho g d}{E_s}\right)^{a_7}(\varphi)^{a_8}(n)^{a_9}(\omega)^{a_{10}} \tag{21}$$

Physically, the total capacity comprises a monopile component (Q_{mono}) and a wing-induced component (Q_{wing}). When $n = 0$ or $B = 0$, $Q_{wing} = 0$. The additive decomposition is

$$\frac{Q_u}{E_s d^2} = C_{mono}.\left(\frac{L}{d}\right)^{a_4}\left(\frac{E_p}{E_s}\right)^{a_5}\left(\frac{c}{E_s}\right)^{a_6} + C_{wing}\left(\frac{B}{d}\right)^{a_1}\left(\frac{h}{d}\right)^{a_2}\left(\frac{L}{d}\right)^{a_4}\left(\frac{E_p}{E_s}\right)^{a_5}\left(\frac{c}{E_s}\right)^{a_6}(n)^{a_9} \tag{22}$$

where the constant terms $\frac{b_f}{d} = 0.14$, $\varphi(20^\circ)$, and ω are absorbed into C_{mono} and C_{wing}. Because $\pi_{12} = \frac{h_w}{d}$ is excluded from the regression, $a_{11} = 0$ in the power law form, and the embedment optimum is discussed as an observation specific to the investigated baseline configuration.

The final calibrated expression retains an explicit gravity correction on the monopile contribution,

$$Q_u = E_s d^2\left[C_{mono}.\left(\frac{L}{d}\right)^{a_4}\left(\frac{E_p}{E_s}\right)^{a_5}\left(\frac{c}{E_s}\right)^{a_6}\left(\frac{\rho g d/E_s}{\rho g d/E_{s,ref}}\right)^{a_7} + C_{wing}.\left(\frac{B}{d}\right)^{a_1}\left(\frac{h}{d}\right)^{a_2}\left(\frac{L}{d}\right)^{a_4}\left(\frac{E_p}{E_s}\right)^{a_5}\left(\frac{c}{E_s}\right)^{a_6}(n)^{a_9}\right] \tag{23}$$

For the reduced-scale baseline model, since $\gamma = \rho g$, the gravity correction factor G is given by

$$G = \left(\frac{\pi_8}{\pi_{8,\mathrm{ref}}}\right)^{a_7}, \pi_{8,\mathrm{ref}} = \frac{\rho g d}{E_{s,\mathrm{ref}}} = \frac{\left(1750\ \mathrm{kg/m^3}\right)\left(9.81\ \mathrm{m/s^2}\right)(0.10\ \mathrm{m})}{20 \times 10^6\ \mathrm{Pa}} = 8.58 \times 10^{-5} \tag{24}$$

The nine parameters in Table 12 (C_{mono}, C_{wing}, a_1, a_2, a_4, a_5, a_6 a_7, a_9) were determined by nonlinear least-squares regression and full-scale calibration, as described in Sections 4.3 and 4.4.

Table 12. Calibrated coefficients of the dimensionless bearing capacity formula.

Parameter	Symbol	Value	Interpretation
Monopile constant	C_{mono}	0.3094	Baseline shaft + tip capacity
Wing constant	C_{wing}	0.1805	Wing–soil interaction contribution
Wing projection	a_1	0.8754	Dominant geometric parameter
Wing height	a_2	0.1321	Secondary influence
Pile slenderness	a_4	0.1037	Moderate positive effect
Stiffness ratio	a_5	0.1001	Small positive effect
Cohesion ratio	a_6	0.4850	Strongest soil parameter
Gravity–stress scale exponent	a_7	0.44	Calibrated from FS-M full-scale monopile (Section 4.4)
Wing number	a_9	0.7222	Near-linear increase with

4.2. Regression Methodology

The eight regression coefficients in Table 12 (excluding a_7, which was calibrated separately from FS-M) were determined by nonlinear least-squares regression using the Levenberg–Marquardt algorithm implemented in MATLAB (R2026a, MathWorks, Natick, MA, USA). The objective function minimized the sum of squared residuals between the predicted and actual dimensionless bearing capacity $\pi_1 = Q_u/(E_s d^2)'$,

$$S = \sum_{i=1}^{N} \left[\pi_{i,\text{pred}} - \pi_{i,\text{actial}} \right]^2 \tag{25}$$

where $N = 16$ is the number of parametric cases. The Jacobian matrix was computed numerically via central finite differences. Convergence was declared when the relative change fell below 10^{-12}. Model performance was assessed in-sample by the coefficient of determination R^2 and the mean absolute percentage error (MAPE), and predictively by leave-one-out cross-validation (LOOCV, Section 4.3), with the bounded parameterization ensuring stable fold-wise re-fitting.

4.3. Regression Results

The calibrated regression coefficients are summarized in Table 12. It is emphasized that the LOOCV folds operate exclusively on the 16 reduced-scale parametric cases; the FS-M full-scale reference is outside this procedure. These in-sample statistics characterize the fit of the eight regression coefficients; the scale exponent a_7 was determined independently and is therefore not included in this calibration error metric. Because wing embedment depth is discussed as an observation specific to the investigated baseline rather than an explicit term in the formulation (Section 3.5), residual variance is predominantly driven by the two embedment variation cases (ED80 and ED180), whose deviations directly reflect the embedment penalties quantified in Section 3.5 (−8.8% and −16.1%, respectively). The higher LOOCV error for configuration ED180 ($h_w/d = 1.8$) stems from the absence of an explicit embedment term in the formulation. The formula is referenced to the observed baseline optimum ($h_w/d \approx 1.3$), and the documented −16.1% penalty at $1.8d$ is a finite-element result rather than a capacity loss directly predicted by the equation for the withheld case. Among the fitted power exponents, the wing projection exponent ($a_1 = 0.8754$) emerges as the dominant geometric parameter, followed by the cohesion ratio exponent ($a_6 = 0.4850$). The wing number exponent ($a_9 = 0.7222$) reflects a sub-linear capacity scaling with the number of wings (n), capturing the diminishing marginal gains observed beyond $n = 2$ (Section 3.5). Conversely, the comparatively small wing height exponent ($a_2 = 0.1321$) confirms that mobilized lateral resistance is primarily governed by the horizontal projection of the wing rather than its vertical dimension along the pile shaft.

The governing formulation adopts a conventional multiplicative (separable) Buckingham π power law structure, assigning a unique scaling exponent to each independent dimensionless group. The prototype-scale finite element predictions in Section 4.4 provide limited numerical support for this separability assumption within the investigated parameter combinations. Furthermore, a systematic evaluation of potential coupled interaction terms across an expanded parametric database is identified as an objective for future research. Given that the calibration dataset comprises 16 simulations relative to eight regression coefficients (a_7 excluded), in-sample statistics characterize calibration goodness-of-fit rather than independent predictive generalization. To evaluate out-of-sample robustness and safeguard against potential overfitting, leave-one-out cross-validation (LOOCV) was performed; the equation was iteratively re-fitted 16 times, each time withholding a single observation for blind prediction. The resulting cross-validation metrics (Table 10) demonstrate strong predictive fidelity, achieving an out-of-sample $R^2 = 0.872$ and an overall

MAPE = 4.66% across all 16 folds, which reduces to 2.89% across the 13 core cases. The three boundary folds—WP0 (the baseline monopile used to distinguish the shaft contribution, whose LOOCV prediction is sensitive to numerical initialization) and ED80/ED180 (embedment configurations whose capacity variation is not explicitly represented by the equation)—account for the larger deviations shown in Figure 18.

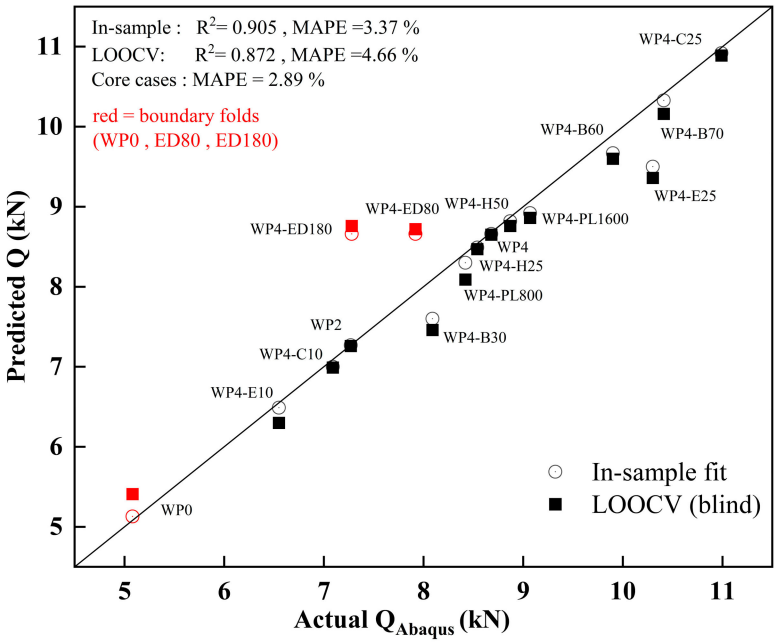


Figure 18. In-sample fit (open circles) and LOOCV (filled squares) of the 9-parameter capacity equation. Statistics: in-sample R^2 = 0.905, MAPE = 3.37%; LOOCV MAPE = 4.66% (2.89% excluding WP0, ED80 and ED180). Solid line: 1:1.

4.4. Scale Effects and Prototype-Scale Numerical Comparisons

Reduced-scale physical modeling enforces similitude with the prototype via invariant dimensionless groups, preserving identical geometric ratios (B/d, h/d, L/d) and stiffness/strength ratios (E_p/E_s, c/E_s) across both scales. However, geometric and material similarity do not equate to strict stress similarity: because self-weight stresses cannot be scaled in a 1 g environment, the gravity–stress ratio ($\pi_8 = \rho g d/E_s$) increases by an order of magnitude (8–10 times) from model to prototype. To represent this scaling disparity in the investigated numerical cases, the governing formulation Equation (23) incorporates a normalized gravity–stress correction factor, $(\pi_8/\pi_{8,\mathrm{ref}})^{a_7}$, applied directly to the monopile term only. The scaling exponent was calibrated using only one full-scale numerical reference monopile (FS-M). The remaining eight winged pile configurations were excluded from this scale calibration and are treated as finite-element blind predictions. FS-M is a calibration case and is excluded from that prediction set.

The gravity factor (G) applies only to the monopile term because shaft friction and toe resistance scale directly with depth-dependent overburden stress ($\sigma_v' = \gamma z$). Conversely, wing resistance is mobilized by shallow passive pressure governed by soil strength (c, φ) and wing geometry (B, h) rather than the vertical stress gradient. The scaling exponent a_7 appears explicitly in G, which multiplies the monopile contribution in Equation (23); the fitted monopile constant (C_{mono}) remains separate from this explicit correction. Applying G only to the monopile contribution is the adopted scaling representation assessed against the reported numerical cases.

It is noted that the scale exponent is determined from a single full-scale monopile reference condition (FS-M). While this provides one numerical calibration anchor for

gravity correction, its reliability is inherently limited to the parameter domain investigated; extension to markedly different soil stiffnesses, pile diameters, or gravity environments would require additional full-scale calibration points.

To assess this scaling formulation within the investigated numerical domain, eight independent full-scale and intermediate-scale finite element models (Table 13; $d = 800$ mm and 1000 mm; $n = 2, 4$; $h_w/d = 0.5$–2.0), none of which were included in the calibration dataset, were analyzed under the baseline soil state ($c = 15.5$ kPa, $E_s = 20$ MPa), with capacity evaluated at the serviceability limit ($s = 0.1d$). The proposed formulation predicted all eight independent cases within a narrow residual band of −4.4% to +3.4%, achieving an overall mean absolute percentage error (MAPE) of 2.63%. Furthermore, within the four-wing series, varying the relative embedment depth from $h_w/d = 0.5$ to 2.0 altered the computed finite element capacity by less than ±0.7%, showing limited embedment sensitivity in this particular full-scale numerical series.

Table 13. Full-scale and intermediate-scale FE blind predictions (eight cases) calibrated against the FS-M monopile reference. The FS-M served to calibrate a_7 and is excluded from the blind set.

Model	n	h_w/d	d (mm)	L (m)	Q_{FE} (kN)	Q_{Pred} (kN)	Error (%)
FS-4W-2.0	4	2.0	1000	12	1832.53	1752.5	−4.4
FS-4W-1.5	4	1.5	1000	12	1820.73	1752.5	−3.8
FS-4W-1.0	4	1.0	1000	12	1820.63	1752.5	−3.7
FS-4W-0.5	4	0.5	1000	12	1808.28	1752.5	−3.1
FS-2W-1.5	2	1.5	1000	12	1564.33	1616.7	+3.4
FS-2W-1.0	2	1.0	1000	12	1604.73	1616.7	+0.8
FS-2W-1.88-D8	2	1.88	800	10	985.80	988.5	+0.3
FS-2W-1.25-D8	2	1.25	800	10	971.95	988.5	+1.7

It is emphasized that these are finite-element blind predictions, not independent full-scale field tests. They provide numerical comparisons for the scaling framework within the investigated configurations and parameter range, rather than proof that all physical scale dependencies have been corrected. The correction should therefore be regarded as a preliminary calibrated representation of scale effects. Broader engineering application requires further scale calibration and independent full-scale field validation.

The identical predictions for the four-wing family reflect the absence of an embedment term in Equation (23) (Section 3.5). Consequently, the equation yields the same predicted capacity for these configurations, whereas their finite-element capacities vary by approximately ±0.7% around the series mean over the investigated relative embedment depth range of 0.5–2.0. The FS-M served as the calibration anchor and is excluded from the blind prediction set. Table 13 presents the eight independent finite-element blind predictions.

5. Conclusions

This study presents the first systematic investigation into the vertical compressive behavior of I-wing piles situated in collapsible Malan loess. By utilizing a combination of physical model testing, validated 3D finite-element analysis, and dimensional analysis, this research addresses a critical foundational gap for transmission towers in Northwest China. Based on these investigations, the following primary conclusions are drawn:

1. Significant capacity enhancement. The integration of wing plates drastically improves compressive capacity within loess. At a standard settlement criterion of $s = 0.1d$ (10 mm), the four-wing pile (WP4) achieved an ultimate capacity of 8.59 kN in the validated finite-element model (69% improvement over the monopile), while the corresponding measured capacity was 8.20 kN (52% improvement). Similarly, the

two-wing pile (WP2) demonstrated 43% gain in simulation and 36% in physical testing. However, adding further wings yields diminishing returns—doubling the wing count from two to four increased capacity by only an additional 18.2%, as adjacent wings begin to mobilize overlapping volumes of soil;

2. Fundamental shift in load transfer. Wing plates actively alter the foundation's load transfer mechanism. Load decomposition at $s = 0.1d$ demonstrates that while a standard monopile relies predominantly on tip resistance (59.65%), the four-wing configuration effectively redistributes this stress. In the four-wing pile, the base carries only 33.18% of the load, the wings intercept 18.98% of the load in direct bearing, while the side resistance Q_s (shaft + wing-side friction) contributes the largest share (47.85%) for the four-wing pile, versus 40.4% for the monopole, with the wing-side friction within it verified to be negligible (≈0.2%) by direct traction integration (Section 3.4.3). This confirms a fundamental upward shift of the load transfer center away from the pile toe, which successively reduces stress concentration at the pile toe, mitigating the risk of progressive collapse in metastable loess;
3. Validity of the hyperbolic interface model. The standard hyperbolic formulation ($q = w/(a + bw)$) proved effective for modeling all soil–pile components, including the novel wing–soil interface. The model successfully calibrated the shaft ($\tau - z$), base ($q - w$), and wing ($q - w$) responses, achieving values ranging from 0.933 to 0.999 across all interface fits, with the majority exceeding 0.98. The non-physical negative initial stiffness fits at the two deepest elevations were discarded and are not used in any subsequent calculation (see Table 6 and Section 3.4.2 under the heading "Monopile $t - z$ Calibration (Validation Baseline");
4. Dominant geometric parameters. Wing projection and wing count serve as the primary drivers of structural capacity. Parametric studies indicate that wing projection (B) provides an almost linear boost to capacity (exponent $a_1 = 0.8754$), whereas variations in wing height (h) exert a negligible influence (less than ±2.2%). Furthermore, an optimal wing embedment depth was identified at $h_w/d \approx 1.3$ for the investigated reduced-scale baseline configuration. This observed optimum is not a universal design rule. The formula has no explicit embedment term and cannot directly predict off-optimum capacity losses; [0.8, 1.8] is the tested interval, not a validated prediction range. In the investigated full-scale finite-element series, varying embedment from $h_w/d = 0.5$ to 2.0 alters capacity by less than ±0.7%, indicating secondary embedment sensitivity in that particular numerical series. Shallower placements cause premature surface yielding, while deeper placements induce shaft drag-down effects that ultimately limit wing mobilization;
5. Derivation of a unified dimensionless capacity expression. Applying Buckingham's π theorem, a nine-parameter dimensionless capacity expression was developed, comprising eight regression coefficients and one independently calibrated gravity-scaling exponent (Table 12). Multivariate regression against the sixteen-case parametric database yielded an in-sample coefficient of determination of $R^2 = 0.905$ and a mean absolute percentage error of MAPE = 3.37%. The sixteen-case parametric matrix isolates single-factor main effects; potential interaction terms between geometric and material parameters are not explicitly quantified, and the fitted model assumes multiplicative separability beyond the calibrated domain. Wing embedment depth is retained as an observation specific to the investigated baseline rather than an explicit regression parameter. Leave-one-out cross-validation (LOOCV) was used to assess predictive performance within the available numerical dataset. Iteratively re-fitting the equation across 16 folds produced an out-of-sample MAPE = 4.66% (which drops to 2.89% when excluding the three documented boundary folds). Furthermore, eight indepen-

dent prototype winged pile configurations (full-scale and intermediate-scale FE models not included in the reduced-scale regression) exhibited close agreement within −4.4% to +3.4% (MAPE = 2.63%). These numerical comparisons support the formulation within the investigated model and parameter domain, but do not establish general scale transferability or replace independent full-scale field validation. The full-scale monopile reference (FS-M) served to calibrate the gravity-scaling exponent a_7 and is therefore distinguished from the blind predictions. The gravity–stress correction exponent ($a_7 = 0.44$) was uniquely anchored to the full-scale benchmark monopile (FS-M) and incorporated via a normalized gravity–stress ratio. Its reliability is inherently limited to the parameter domain investigated; extension to markedly different soil stiffnesses, pile diameters, or gravity environments would require additional full-scale calibration points. The parametric sensitivity analysis identified the wing projection exponent ($a_1 = 0.8754$) as the dominant geometric parameter, with the wing number exponent ($a_9 = 0.7222$) reflecting the near-linear capacity scaling with n, the cohesion ratio exponent ($a_6 = 0.4850$) the strongest soil parameter, and the wing height exponent ($a_2 = 0.1321$) of comparatively small influence—confirming that mobilized resistance is governed primarily by the wing's horizontal projection rather than its vertical dimension.

From an engineering perspective, the proposed dimensionless expression provides a preliminary numerical capacity-estimation framework for transmission tower foundations in loess, with applicability currently limited to the investigated models and parameter ranges. Because the current study was conducted using reduced-scale models under dry loessial conditions, the numerical assessment of the formula is limited to dry, non-wetted, compacted Malan loess, and cannot be directly extended to water-immersion, wetting-induced collapse, or suction change scenarios without additional hydro-mechanically coupled modeling and experimental validation. Future research must expand to full-scale field testing and investigate foundational behavior under wetting-induced collapse, suction loss and negative skin friction, and thoroughly examine combined loading scenarios such as lateral, uplift, and moment forces, which are highly typical of transmission tower foundations subjected to wind and cable tension.

Author Contributions: Conceptualization, F.T. and Q.S.; methodology, F.T. and Q.S.; software, P.Z.; validation, F.T., G.Z. and P.Z.; formal analysis, F.T. and Y.G.; investigation, F.T. and Y.G.; resources, G.Z. and F.W.; data curation, F.T. and P.Z.; writing—original draft preparation, F.T.; writing—review and editing, Q.S. and G.Z.; visualization, F.T. and P.Z.; supervision, Q.S.; project administration, G.Z.; funding acquisition, F.T. All authors have read and agreed to the published version of the manuscript.

Funding: This research was funded by the Science and Technology Project of State Grid Shaanxi Electric Power Co., Ltd. (grant number 5226JY250002).

Institutional Review Board Statement: Not applicable.

Informed Consent Statement: Not applicable.

Data Availability Statement: The experimental and numerical data reported in this study are provided in the text, figures, and tables of this article.

Acknowledgments: The authors would like to express their sincere gratitude to the State Grid Shaanxi Electric Power Company Economic and Technological Research Institute, Xi'an 710065, China, and the Northwest Electric Power Design Institute Co., Ltd. of China Power Engineering Consulting Group for their valuable support and collaboration throughout this research. The contributions and technical assistance provided by these institutions greatly facilitated the completion of this study. The authors also acknowledge the support from the research teams involved in the experimental investigation, numerical simulation, and data analysis. Furthermore, the authors would like to thank all colleagues who provided constructive suggestions and assistance during the development of this work.

Conflicts of Interest: Authors Fanli Tang, Gang Zhao, Peng Zhang, and Yuhang Guo were employed by the State Grid Shaanxi Electric Power Company Economic and Technological Research Institute, Xi'an 710065, China, and Fan Wen was employed by the Northwest Electric Power Design Institute Co., Ltd. of China Power Engineering Consulting Group. The remaining author declares that the research was conducted in the absence of any commercial or financial relationships that could be construed as a potential conflict of interest.

References

1. Qi, X.; Wang, H.; Xiong, X.; Zhou, A.; Sun, Q.; Zhang, Q. Digital Twin Framework for Structural Health Monitoring of Transmission Towers: Integrating BIM, IoT and FEM for Wind–Flood Multi-Hazard Simulation. *Appl. Sci.* **2026**, *16*, 3620. [CrossRef]
2. Yang, J.-G.; Li, S.; Zhou, C.-G.; Li, L.-Y.; Tian, B.; Yang, W.-G.; Zhang, S.-H. Response of Transmission Tower Guy Wires Under Impact: Theoretical Analysis and Finite Element Simulation. *Appl. Sci.* **2026**, *16*, 123. [CrossRef]
3. Council, C.E. *Annual Development Report of China's Electric Power Industry 2025*; China Electric Power Press: Beijing, China, 2025.
4. Qin, W.; Yao, J.; Liu, Z.; Guo, Y.; Shen, G.; Tu, Z. Structural response and failure analysis of transmission towers under foundation sliding with consideration of wind effects. *Energies* **2025**, *18*, 2878. [CrossRef]
5. Feng, Z.; Hu, H.; Dong, Y.; Wang, F.; Jia, M.; Zhao, Y.; He, J. Effect of Steel Casing on Vertical Bearing Characteristics of Steel Tube-Reinforced Concrete Piles in Loess Area. *Appl. Sci.* **2019**, *9*, 2874. [CrossRef]
6. Gao, D.; Zhao, K.; Ma, B.; Han, Z.; Fan, J. Research on the bearing behavior of single pile in self-weight collapsible loess areas. *PLoS ONE* **2023**, *18*, e0290878. [CrossRef] [PubMed]
7. Wang, X.; Wang, X.; Li, J.; Liu, D.; Zhang, Y.; Jiang, D. Field Test Study of Performance of Bored Piles in Collapsible Loess. *Appl. Sci.* **2023**, *13*, 13113. [CrossRef]
8. Zhao, Z.; Ye, S.; Zhu, Y.; Tao, H.; Chen, C. Scale model test study on negative skin friction of piles considering the collapsibility of loess. *Acta Geotech.* **2022**, *17*, 601–611. [CrossRef]
9. Ma, H.; Ma, Y.; Zhu, L.; Zhang, H. Experimental Study on the Difference Mechanism of Shaft Resistance between Uplift Piles and Compressive Piles. *Appl. Sci.* **2023**, *13*, 3158. [CrossRef]
10. Tian, Y.; Zhou, Z.; Dong, Y.; Wang, K.; Feng, H. Study on the value of side friction of bored pile in loess area considering the influence of length diameter ratio. *Arab. J. Geosci.* **2021**, *14*, 2067. [CrossRef]
11. Khan, H.; Hu, Z.; Alshawmar, F.; Olusegun, V.T. Bearing mechanism and design optimization of screw piles in loess area. *Sci. Rep.* **2026**, *16*, 21631. [CrossRef] [PubMed]
12. Zhu, Y.; Cao, W.; Lyu, P.; Wang, Y.; Zhao, M. Bearing behavior of inclined pile for transmission towers in loess soils under immersion. *China Saf. Sci. J.* **2025**, *35*, 169–178.
13. Gao, X.; Xie, W.; Yuan, K.; Liu, Q. Mechanical properties and microstructural evolution of Malan loess with depth: Insights from multivariate statistical models. *Soil Tillage Res.* **2025**, *251*, 106548. [CrossRef]
14. Yuan, K.; Ni, W.; Lü, X.; Zhu, M.; Wang, H.; Nie, Y. Mechanical properties and microstructure evolution of Malan loess. *Quat. Int.* **2022**, *637*, 74–84. [CrossRef]
15. Potyondy, J.G. Skin Friction between Various Soils and Construction Materials. *Géotechnique* **1961**, *11*, 339–353. [CrossRef]
16. Nasr, A.M.A. Experimental and theoretical studies of laterally loaded finned piles in sand. *Can. Geotech. J.* **2014**, *51*, 381–393. [CrossRef]
17. Abongo, K.; Gu, J.; Pervizpour, M.; Quiel, S.; Pamukcu, S. Parametric lab-scale testing and numerical simulation of finned monopiles under directional loading. *Ocean Eng.* **2022**, *259*, 111871. [CrossRef]
18. Jayashree, J.; Sathyapriya, S. Load sharing behaviour of bio-inspired root pile foundation in cohesionless soil under individual and combined loading conditions. *Sci. Rep.* **2025**, *15*, 5440. [CrossRef] [PubMed]
19. Albusoda, B.S.; Al-Saadi, A.F.; Jasim, A.F. An experimental study and numerical modeling of laterally loaded regular and finned pile foundations in sandy soils. *Comput. Geotech.* **2018**, *102*, 102–110. [CrossRef]
20. Vignesh, V.; Muthukumar, M. Experimental and numerical study of group effect on the behavior of helical piles in soft clays under uplift and lateral loading. *Ocean Eng.* **2023**, *268*, 113500. [CrossRef]
21. Gao, X.-j.; Wang, J.-c.; Zhu, X.-r. Static load test and load transfer mechanism study of squeezed branch and plate pile in collapsible loess foundation. *J. Zhejiang Univ.-Sci. A* **2007**, *8*, 1110–1117. [CrossRef]
22. Mahdi, T.; Al-Neami, M.; Raheel, F. An experimental and theoretical studies wings piles at different sandy soil densities. *Eng. Technol. J.* **2022**, *40*, 1422–1431. [CrossRef]
23. Sakr, M.; Nazir, A.; Azzam, W.; Sallam, A. Model study of single pile with wings under uplift loads. *Appl. Ocean Res.* **2020**, *100*, 102187. [CrossRef]
24. EL-Nemr, M.T.; Azzam, W.R.; Gaber, E.K.; Ashour, O. Numerical investigation of the behavior of group-finned piles in sandy soil subjected to tensile loads. *Nile J. Archit. Civ. Eng.* **2024**, *4*, 1–21. [CrossRef]

25. Yang, H.; Tan, T.; Pan, J.; Wang, C. Research on Improving the Horizontal Bearing Performance of Wind Power Pile Foundation with Added Wing Structure. *Sustainability* **2025**, *17*, 861. [CrossRef]
26. Hao, D.; Zhang, Y.; Chen, Y.; Chen, R.; Kong, G.; Wu, K.; Han, Y. Numerical analysis of bearing capacity of winged helical anchor in clayed soil. *Sci. Rep.* **2025**, *15*, 16380. [CrossRef] [PubMed]
27. Terzaghi, K. *Theoretical Soil Mechanics*; John Wiley & Sons: New York, NY, USA, 1943.
28. *IS 2911 (Part 4): 2013*; Design and Construction of Pile Foundations—Code of Practice, Part 4: Load Test on Piles, 2nd ed. Bureau of Indian Standards (BIS): New Delhi, India, 2013.
29. Buckingham, E. On physically similar systems; illustrations of the use of dimensional equations. *Phys. Rev.* **1914**, *4*, 345. [CrossRef]
30. Butterfield, R. Dimensional analysis for geotechnical engineers. *Géotechnique* **1999**, *49*, 357–366. [CrossRef]
31. Gao, M.; Wang, M.; Jiao, H.; Yin, S. Ultimate bearing capacity formula for large diameter belled piles based on π theorem. *Arab. J. Geosci.* **2021**, *14*, 2830. [CrossRef]
32. Sedran, G.; Stolle, D.F.E.; Horvath, R.G. An investigation of scaling and dimensional analysis of axially loaded piles. *Can. Geotech. J.* **2001**, *38*, 530–541. [CrossRef]
33. *JGJ 94-2008*; Technical Code for Building Pile Foundations. China Architecture and Building Press: Beijing, China, 2008.
34. Tolun, M.; Emirler, B.; Ertugrul, O.L.; Yildiz, A. Effect of dilatancy on tension response of completely rough piles embedded in granular soils. *Ocean Eng.* **2024**, *292*, 116507. [CrossRef]
35. Wang, H.; Bransby, M.F.; Lehane, B.M.; Wang, L.; Hong, Y. Numerical investigation of the monotonic drained lateral behaviour of large-diameter rigid piles in medium-dense uniform sand. *Géotechnique* **2023**, *73*, 689–700. [CrossRef]
36. Xue, X.; Wang, J.; Sheng, M.; Sun, Q. Experimental, Numerical, and Analytical Studies of the Uplift Behavior of Mini-Piles in Moistened Loess Foundations With Parameter Sensitivity Analysis. *Adv. Civ. Eng.* **2026**, *2026*, 8867043. [CrossRef]
37. Zhou, M.; Xing, L.; Chen, Y.; Qiao, H. Settlement characteristics of split grouting pile composite foundation in loess areas. *Adv. Civ. Eng.* **2022**, *2022*, 8627124. [CrossRef]
38. Vermeer, P.A.; de Borst, R. Non-associated plasticity for soils, concrete and rock. *Heron* **1984**, *29*, 1–64.
39. Bolton, M. The strength and dilatancy of sands. *Geotechnique* **1986**, *36*, 65–78. [CrossRef]
40. Li, Y.; Xu, S.; Liu, H.; Ma, E.; Wang, L. Displacement and Stress Characteristics of Tunnel Foundation in Collapsible Loess Ground Reinforced by Jet Grouting Columns. *Adv. Civ. Eng.* **2018**, *2018*, 2352174. [CrossRef]
41. Ye, S.; Xin, L.; Cui, X.; Zhang, W.; Wu, J. Modelling pile-soil interaction and bearing capacity assessment of super-long piles in loess. *Geomech. Geoengin.* **2026**, *21*, 1180–1204. [CrossRef]
42. *GB 50010-2010*; Code for Design of Concrete Structures. China Architecture & Building Press: Beijing, China, 2010.
43. *GB/T 700-2006*; Carbon Structural Steels. Standards Press of China: Beijing, China, 2006.
44. Hossain, M.A.; Yin, J.-H. Behavior of a pressure-grouted soil-cement interface in direct shear tests. *Int. J. Geomech.* **2014**, *14*, 101–109. [CrossRef]
45. Kadhim, H.K.; Alyounis, M. Effect of surface roughness on interface shear strength parameters of sandy soils. *Open Eng.* **2024**, *14*, 20240018. [CrossRef]
46. Wang, G. Research on the Method of Ground Stress Balance under Complex Conditions Based on Geometric Tracing. *Adv. Civ. Eng.* **2022**, *2022*, 9359268. [CrossRef]
47. Wang, X.-Y.; Yuan, Y.-L.; Hu, C.-M.; Mei, Y. Research on the Geostatic Stress Field Procedure under Complex Conditions. *Adv. Civ. Eng.* **2021**, *2021*, 6674369. [CrossRef]
48. Franza, A.; Marshall, A.M. Centrifuge modelling of tunnelling beneath axially loaded displacement and non-displacement piles in sand. In *Geotechnical Frontiers 2017*; ASCE: Reston, VA, USA, 2017; pp. 576–586.
49. Leong, W.K.; Yusoff, N.A.; Aziz, A.N.A.; Talib, Z.A. Theoretical and Actual Bearing Capacity of Driven Piles Using Model Piles in Sand. In *International Integrated Engineering Summit 2014*; Applied Mechanics and Materials; Trans Tech Publications Ltd.: Bäch, Switzerland, 2015; pp. 1453–1459.
50. Jalali, U.H.; Alshameri, B.; Khalid, M.H.; Hassan, W.; Abdeldjouad, L.; Jamil, S.M.; Farooq, H.; Maqsood, Z. Data-driven approach to enhance deep foundation safety: Reliable methods for predicting bored pile capacity. *Int. J. Geo-Eng.* **2025**, *16*, 16. [CrossRef]
51. Malik, A.A.; Kuwano, J.; Tachibana, S.; Maejima, T. Interpretation of screw pile load test data using extrapolation method in dense sand. *Int. J. GEOMATE* **2016**, *10*, 1567–1574. [CrossRef]
52. Cheng, J.; Tong, L.; Sun, C.; Zhu, H.; Deng, J. Experimental and numerical simulation investigations on the bearing capacity of stepped variable-section DX piles under vertical loading. *Buildings* **2024**, *14*, 3078. [CrossRef]
53. Seed, H.B.; Reese, L.C. The action of soft clay along friction piles. *Trans. Am. Soc. Civ. Eng.* **1957**, *122*, 731–754. [CrossRef]
54. Fleming, W. A new method for single pile settlement prediction and analysis. *Geotechnique* **1992**, *42*, 411–425. [CrossRef]
55. Cao, W.; Chen, Y.; Wolfe, W. New load transfer hyperbolic model for pile-soil interface and negative skin friction on single piles embedded in soft soils. *Int. J. Geomech.* **2014**, *14*, 92–100. [CrossRef]
56. Zhou, P.; Li, J.-P.; Li, P.-P.; Liu, G.-Y.; Zhang, C.-Z. Prediction method for load-settlement response of a single pile in sand based on an interface constitutive model. *Rock Soil Mech.* **2024**, *45*, 1686–1698. [CrossRef]

57. Das, B.M.; Sivakugan, N. *Principles of Foundation Engineering*; Cengage Learning: Boston, MA, USA, 2018.
58. Al-Baidhani, A.F.; Al-kifae, A.A.A. Influence of Geometric Configuration on Load-Bearing Capacity of Under-Reamed Piles in Saturated and Partially Saturated Clay–Experimental Work. *F1000Research* **2026**, *15*, 1041. [CrossRef]

Disclaimer/Publisher's Note: The statements, opinions and data contained in all publications are solely those of the individual author(s) and contributor(s) and not of MDPI and/or the editor(s). MDPI and/or the editor(s) disclaim responsibility for any injury to people or property resulting from any ideas, methods, instructions or products referred to in the content.